



HAL
open science

Architecture Design and Ground Performance of Netherlands-China Low-Frequency Explorer

Sukanth Karapakula, Christiaan Brinkerink, Antonio Vecchio, Hamid R. Pourshaghghi, Peter Dolron, Roel Jordans, Eric Bertels, Gerard Aalbers, Mark Ruiter, Albert J. Boonstra, et al.

► **To cite this version:**

Sukanth Karapakula, Christiaan Brinkerink, Antonio Vecchio, Hamid R. Pourshaghghi, Peter Dolron, et al.. Architecture Design and Ground Performance of Netherlands-China Low-Frequency Explorer. Radio Science, 2024, 59, 10.1029/2023RS007906 . insu-04853422

HAL Id: insu-04853422

<https://insu.hal.science/insu-04853422v1>

Submitted on 23 Dec 2024

HAL is a multi-disciplinary open access archive for the deposit and dissemination of scientific research documents, whether they are published or not. The documents may come from teaching and research institutions in France or abroad, or from public or private research centers.

L'archive ouverte pluridisciplinaire **HAL**, est destinée au dépôt et à la diffusion de documents scientifiques de niveau recherche, publiés ou non, émanant des établissements d'enseignement et de recherche français ou étrangers, des laboratoires publics ou privés.



Distributed under a Creative Commons Attribution 4.0 International License



Architecture Design and Ground Performance of Netherlands-China Low-Frequency Explorer

Key Points:

- Radio observations from the Moon at very low frequencies
- Radio instrument technology demonstration for future lunar observatory and interferometry
- Radio receiver design for low-frequency observation

Correspondence to:







S. Karapakula,
s.karapakula@astro.ru.nl

Citation:

Karapakula, S., Brinkerink, C., Vecchio, A., Pourshaghghi, H. R., Dolron, P., Jordans, R., et al. (2024). Architecture design and ground performance of Netherlands-China Low-Frequency Explorer. *Radio Science*, 59, e2023RS007906. <https://doi.org/10.1029/2023RS007906>

Received 23 NOV 2023

Accepted 10 JUL 2024

Sukanth Karapakula¹ , Christiaan Brinkerink¹ , Antonio Vecchio^{1,2}, Hamid R. Pourshaghghi¹, Peter Dolron¹, Roel Jordans^{1,3}, Eric Bertels⁴, Gerard Aalbers⁴, Mark Ruiter⁵, Albert J. Boonstra⁵ , Mark Bentum^{3,5}, David Prinsloo^{3,5}, Michel Arts⁵ , Jeanette Bast⁵, Sieds Damstra⁵, Albert van Duin⁵, Nico Ebbendorf⁵, Hans van der Marel⁵, Juergen Morawietz⁵, Roel Witvers⁵, Wietse Poiesz⁶, Rico van Dongen⁶, Baptiste Cecconi² , Philippe Zarka² , Moustapha Dekkali², Linjie Chen^{7,8}, Mingyuan Wang⁷, Mo Zhang⁷, Maohai Huang⁷, Yihua Yan^{7,8}, Liang Dong⁹, Baolin Tan⁷, Lihua Zhang¹⁰, Liang Xiong¹⁰, Ji Sun¹⁰, Hongbo Zhang⁷, Jinsong Ping⁷, Marc Klein Wolt¹, and Heino Falcke¹

¹Radboud Radio Lab, Department of Astrophysics/IMAPP, Radboud University, Nijmegen, The Netherlands, ²LESIA, Observatoire de Paris, Université PSL, CNRS, Sorbonne Université, Univ. Paris Didero, Meudon, France, ³Faculty of Electrical Engineering, Eindhoven University of Technology, Eindhoven, The Netherlands, ⁴ISISpace Innovative Solutions in Space, Delft, The Netherlands, ⁵Netherlands Institute for Radio Astronomy (ASTRON), Dwingeloo, The Netherlands, ⁶Inspiro BV, Arnhem, The Netherlands, ⁷National Astronomical Observatories, Chinese Academy of Sciences, Beijing, China, ⁸National Space Science Center, Chinese Academy of Sciences, Beijing, China, ⁹Yunnan Observatories, Chinese Academy of Sciences, Kunming, China, ¹⁰DFH Satellite Co., Ltd., Beijing, China

Abstract The Netherlands-China Low-Frequency Explorer (NCLE) (Boonstra et al., 2017, [https://www.ursi.org/proceedings/procGA17/papers/Paper_J19-2\(1603\).pdf](https://www.ursi.org/proceedings/procGA17/papers/Paper_J19-2(1603).pdf); Chen et al., 2020, <https://ui.adsabs.harvard.edu/abs/2020AAS...23610203C/abstract>) is a radio instrument for astrophysical studies in the low-frequency range (80 kHz–80 MHz). As a technology demonstrator, NCLE shall inform the design of future radio receivers that aim at low-frequency radio astronomy. NCLE can make observations at very high spectral resolution (<1 kHz) and generate radio sky maps at an angular resolution of ≈ 1.5 radians. NCLE uses three monopole antennas, each 5 m long, and three identical analog signal chains to process the signal from each antenna. A single digital receiver samples the signal and calculates the auto-correlated and cross-correlated spectra. The instrument's analog and digital signal chains are extensively configurable. They can be fine-tuned to produce broadband spectra covering the instrument's complete operating frequency range or sub-bands. NCLE was developed within a very short timescale of 2 years, and currently, it is on board Queqiao, the relay spacecraft of the Chang'e-4 mission, in a halo orbit around the Earth-Moon L2 point. This paper outlines the science cases, instrument architecture with focus on the signal chain, and discusses the laboratory measurements during the pre-launch phase.

1. Introduction

Observations at low radio frequencies offer a unique channel to observe the processes of structure formation in the early Universe, through capturing the highly redshifted 21-cm signal from neutral hydrogen. Three timeframes are identified in this context: the epoch before the first stars and galaxies formed (Dark Ages, DA), the epoch when the first stars became active (Cosmic Dawn, CD), and the epoch when much of the neutral hydrogen was reionized (Epoch of Reionisation, EoR). These astrophysical studies require observation at lower frequencies than those penetrating the Earth's ionosphere (Condon & Ransom, 2016; Kelley, 2009; Rishbeth & Garriott, 1969; Wilson et al., 2013). Radio waves cannot propagate at frequencies below the plasma frequency. For the Earth's ionosphere the plasma frequency is typically near 10 MHz by day and 5 MHz by night (the plasma frequency can reach somewhat lower values near the Earth's magnetic poles), implying that all frequencies near and below these frequencies are cut off and the ionosphere turns completely opaque (Cordes, 1990; Cordes, 2000; Intema et al., 2009; Thompson et al., 2001). The current generation of receivers in ground-based radio telescopes have been enriched to extend the observable lower frequencies from the ground to as low as 10 MHz. These include facilities such as GMRT (<http://www.gmrt.ncra.tifr.res.in>) (Swarup et al., 1991), MWA (<http://www.haystack.mit.edu/ast/arrays/mwa/>) (Morales, 2005; Morales et al., 2006), PAPER (Backer et al., 2007), the low-frequency radio telescope of SKALA (<http://www.skatelescope.org>) (Carilli & Rawlings, 2004; de Lera Acedo et al., 2015;

© 2024. The Author(s).

This is an open access article under the terms of the [Creative Commons Attribution License](https://creativecommons.org/licenses/by/4.0/), which permits use, distribution and reproduction in any medium, provided the original work is properly cited.

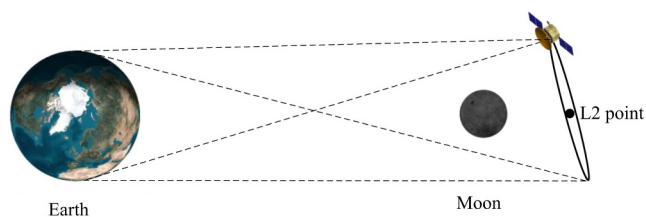


Figure 1. The line-of-sight visibility between the Earth and relay satellite around the lunar L2 Point. [source taken from: Wang and Liu (2016)].

Schilizzi, 2004), LOFAR (<http://www.lofar.org>) (Falcke et al., 2006; Rottgering et al., 2006; van Haarlem et al., 2013) Low Band Antenna (LBA) and NenuFAR (Zarka, 2020).

Performing astrophysical radio observations below the ionospheric cutoff is only possible from space. RAE 1 and 2 studies ((Alexander et al., 1975; Benediktov et al., 1965; Gurnett, 1974; Kaiser, 1987) see Figure 5 from Alexander et al. (1975)) showed that a suitable place in space for low-frequency radio astronomy is on the far side of the Moon, preferably on the Moon's surface. The absence of a permanent ionosphere and the fact that this region is shielded from Earth RFI makes it an attractive location for obser-

ations, and this opens a spectral window that is entirely inaccessible from the Earth's surface, potentially to wavelengths as much as two orders of magnitude longer than those accessible from the ground. Zarka et al. (2012); Cecconi et al. (2012) presented several planetary and exoplanetary science cases that can be done on the far-side surface of the Moon with Low-frequency radio astronomy. Meanwhile, several planetary and Solar missions carried radio instruments, such as the RPW instrument on Cassini (Cecconi et al., 2012; Zarka et al., 2004), WAVES instrument on the WIND satellite (Bougeret et al., 1995), WAVES instrument on STEREO spacecraft (Bougeret et al., 2008), and Solar Orbiter Radio and Plasma Waves (RPWS) (Maksimovic et al., 2021) have contributed significantly toward the advancement of low-frequency (sub-kilohertz to MHz) radio receivers. With the idea of returning to the Moon for astronomical observations, there are several technology demonstrators and pre-cursor missions planned including NCLE, such as ROLSES (Burns, 2024; Burns et al., 2023), LuSEE-Night (Bale et al., 2023; Kassim & Weiler, 1990), Lunar Crater Radio Telescope (Goel et al., 2022), Radio Frequency Spectrometer (RFS) a part of the FIELDS suite for Solar Probe Plus (SPP) (Pulupa et al., 2017), and the Ultra-Long-Wavelength (ULW)—Low Frequency Interferometer and Spectrometer (LFIS) on board the selenocentric satellite Longjiang-2 (Yan et al., 2023).

The Netherlands-China Low-Frequency Explorer (NCLE) (Boonstra et al., 2017; Chen et al., 2020) is a low-frequency radio instrument developed and built by a Dutch consortium. Radboud University is responsible for developing digital receivers and mission design, ISISpace for antenna development, power, and command handling, and ASTRON for low noise amplifier design. NCLE was developed in response to a Chinese call for payloads that could be included on a Moon mission (Chang'e-4). Chang'e 4 is a lunar far-side mission comprising a lander, rover, and relay spacecraft (launched on 21 May 2018). NCLE is the only science instrument on Queqiao, the relay satellite of the Chang'e-4 mission. The maximum allowed payload mass budget for NCLE was 10 kg and a power budget of 50 W. Queqiao is in a halo orbit around the Earth-Moon Lagrange Point 2 (L2) point (61,347 km behind the Moon with a semi-major axis of 13,000 km and a period of ≈ 14 days (Wang & Liu, 2016), see Figure 1). This mission offers a quasi-stable halo orbit for a radio instrument in space and the possibility to explore specific science cases that can be done only from space, where the terrestrial RFI is reduced. The advantages of being in lunar orbit were easy injection of the satellite into the orbit, lesser power constraint, direct visibility from Earth for data transfer of large packets, continuous observation, and rotational freedom to point toward a source. However, there are additional advantages of being on the lunar surface; on the surface, the instrument has reduced RFI, a stable platform preferred for long-term observations; on the surface, temperature conditions change slowly with rotation, but the temperature changes in orbit are rapid, the antenna separation is easier on the surface than in orbit. The complexity of antenna deployment methods is higher on the surface than in orbit. Works by Jester and Falcke (2009); Cecconi et al. (2012); Zarka et al. (2012); Klein Wolt et al. (2012) extensively reviewed these scientific objectives and their operational requirements, noting that they could be observed using a lunar-based Low-Frequency radio array. These investigations, along-side the mission definition of Farside Explorer (Mimoun et al., 2012), served as the framework for NCLE's instrument design.

This paper overviews NCLE's architectural design and delves into the signal chain elements. In Section 2, we present NCLE's science and technical objectives. We present the hardware description of the NCLE sub-systems: in Section 3 the top-level instrument overview, in Section 3.1 the Antenna, in Section 3.2 the Low Noise Amplifier (LNA), the Analog Input Stage (AIS) and the Calibrator, in Section 3.3 the clock & in Section 3.4 the Digital Receiver System (DRS). In Section 4, we present the NCLE data handling operations, and in Section 5, we present the spectra measured on the ground and our conclusions in Section 6.

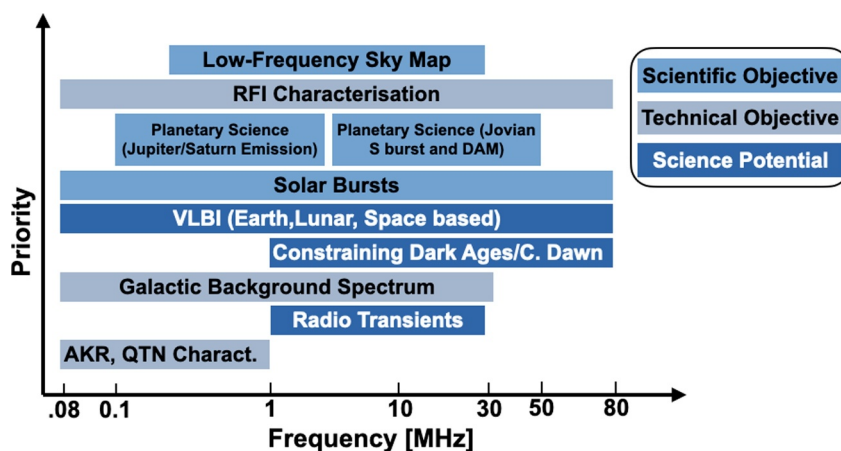


Figure 2. The scientific and technical objectives established by the Netherlands NCLE consortium in the low-frequency domain. At the forefront of our scientific goals is creating a low resolution sky map, representing our highest priority.

2. NCLE Scientific and Technical Objective

The Dutch NCLE consortium defined a set of mission objectives that can be observed from space at low frequencies (<100 MHz) as depicted in Figure 2. These objectives were the foundation for NCLE instrument design, specifically focusing on formulating the sensitivity requirements. The consortium's mission objectives encompassed scientific objectives, technical objectives, and forward-looking science potential categories detailed in Figure 2. *Scientific Objectives:* These objectives were inspired by existing space-based radio instruments and included objectives such as generating low-frequency radio sky maps identifying sources and their brightness as a function of frequency, planetary observations such as Jovian decametric radio emissions (DAM), and studying Solar bursts. *Technical Objectives:* These objectives aimed to address instrumental challenges inherent in low-frequency observations. They encompass studies to characterise instrument sensitivity, calibration techniques, and performance, such as RFI characterisation at the Moon at low frequencies, measurement of Galactic background radiation, Earth's AKR, and the QTN spectrum. *Science Potential:* As part of the consortium's long-term vision, the potential objectives outlined more ambitious goals, including space-based Very Long Baseline Interferometry (VLBI), constraining Dark Ages and Cosmic Dawn signals, and detecting radio transients. In particular, the NCLE hardware is capable of VLBI; however, this functionality would require an in-flight update as it was not included in the flight firmware at launch. VLBI could be performed in conjunction with the low-frequency spectrometer (LFS) present onboard of the Chang'e 4 lander (Jia et al., 2018), or with the LOFAR array on Earth. Target sources for VLBI are those phenomena that are both bright and compact within the frequency range of NCLE: Solar burst emissions around 70 MHz, and beamed Jovian magnetosphere emission (S-bursts) below 40 MHz. Further in this section, the scientific and technical objectives achieved with the completed instrument design are detailed. During the development of NCLE, several possibilities were identified where VLBI might be possible involving stations on Earth (e.g., with LOFAR) or with measurements made from the Moon (the Chang'e 4 lander).

Numerous sources of interest within the Solar system can be observed at low frequencies. A selection of these sources that can be observed with NCLE are presented in Figure 3 (adapted from Figure 3 of Zarka et al. (2012) and the Zarka and Ceconi. (2022) data set). Table 1 shows a summary of the characteristics of these science phenomena in terms of power, polarization, time and frequency. The science requirements are imposed by these characteristics: the lowest power level is found to be $2 \cdot 10^{-25}$ [W/m²/Hz] from the Dark Ages and Cosmic Dawn signals, and the maximum power level is $4 \cdot 10^{-15}$ [W/m²/Hz] from Solar bursts, giving a dynamic range in power of 103 [dB]. The required range of time resolutions for the spectral measurements ranges from a few milliseconds (Jovian S-bursts) up to a few seconds (limited to minimize the risk of interference degrading the data quality).

The system-level design requirements for NCLE are derived from connecting the science phenomena to the technical characteristics needed in order to observe these science cases. From the mission objectives the frequency range of interest has been determined to be 80 kHz to 80 MHz. The science objectives are adapted to these limits. An instantaneous bandwidth maximum of 10 MHz follows from the Jovian S-bursts and the minimum

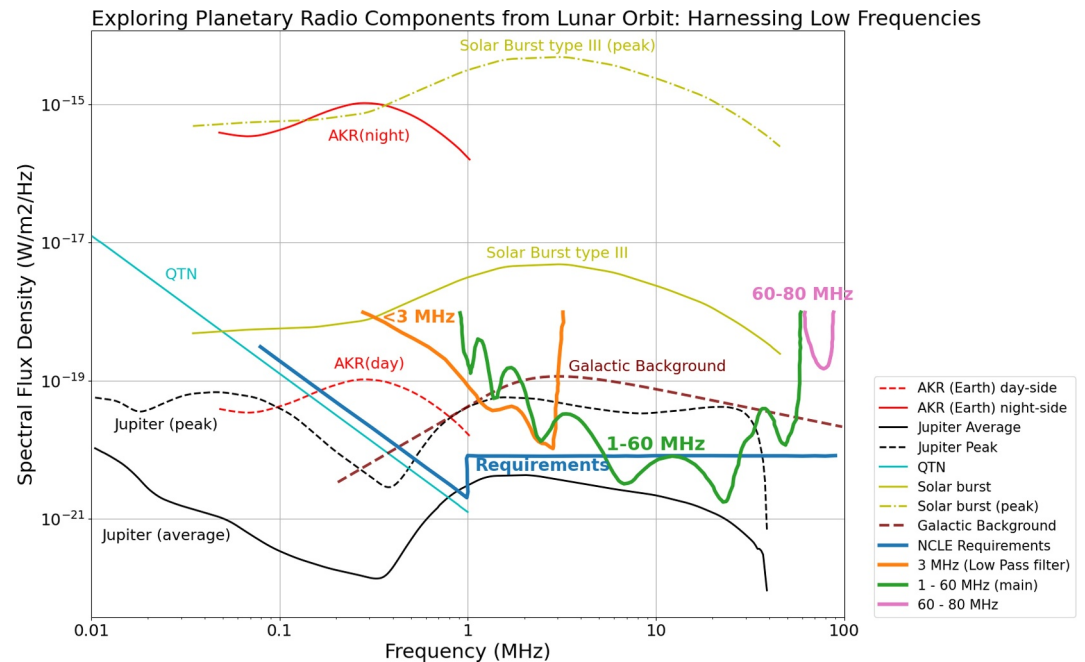


Figure 3. Spectral densities of planetary emissions from a Lunar Orbit can be observed with NCLE operating frequency range of 80 kHz–80 MHz. The plot is adapted from Figure 3 of Zarka et al. (2012) using the Zarka and Ceccconi. (2022) data set. The NCLE Noise Flux Density achieved are depicted for the three operating bands: <3 MHz (orange line), 1–60 MHz (main science band, green line), and 60–80 MHz (pink line). The operating mode of NCLE chooses the frequency range, and the sensitivities depicted in this picture are for an integration time of 1 s. The sources of interest at lower frequencies are AKR—Auroral Kilometric Radiation Earth from day and night side, Solar Burst type III average and peak, Jupiter radio emissions, galactic background, and QTN—Quasi Thermal Noise (depicted equivalent spectral density).

follows from the lowest frequency band used for the sky map objective, which is 10 kHz. The highest spectral resolution required is linked to three science sources: Earth RFI, Earth lightning and Jovian S-bursts. All three of these sources require a spectral resolution of 1 kHz. The minimum temporal resolution of 1 milliseconds is derived from characteristics of Earth Lightning. For non time varying signals it should be possible to split the NCLE band into a number of sub-bands that are measured successively. Which translates to a requirement of number of sub-bands required, bandwidth of these sub-bands and the sampling rate of ADC. The minimum required Power Flux Density (PFD) of $1 \cdot 10^{-20}$ [W/m²/Hz] (from planetary AKR), and a maximum of $4 \cdot 10^{-15}$ [W/m²/Hz] (from Solar bursts) over one second of integration. The design requirement for the NCLE sensitivity (represented by blue line) are derived from Quasi Thermal Noise (QTN) for frequencies below 1 MHz and the galactic background signal for frequencies above 1 MHz.

To meet these system requirement's set by the objectives, three operating bands were designed: the achieved sensitivities are shown in Figure 3 for these bands <3 MHz (represented by orange line), 1–60 MHz (main science band, represented by green line), and 60–80 MHz (represented by pink line). The choice of three bands was influenced by various factors, the most prominent being the instrumental noise at lower frequencies (<1 MHz). Achieving the requirements posed a partial success for the main science band. However, the other two bands presented technical challenges due to the tight development time frame of 2 years. It is worth noting that noise flux density can be improved by increasing integration time, particularly in the case of the primary science band. However, this approach is less effective for the 3 MHz band due to system noise limitations.

One of NCLE's primary objectives is to survey the sky and generate radio sky maps at low-frequency. The Global Sky Model (GSM) by De Oliveira-Costa et al. (2008) is a leading model for the sky in the frequency range of 10–200 MHz. The GSM sky map is modeled from an analysis of 11 sky maps, and only three maps are in the frequency range of 10–200 MHz: 10 MHz (Caswell, 1976), 22 MHz (R. S. Roger et al., 1999) and 45 MHz (H. Alvarez et al., 1997; A. E. Guzman et al., 2011; K. Maeda et al., 1999). The GSM sky maps are extrapolated for other frequencies in the 10–200 MHz range. There are uncertainties in the accuracy of input maps at the three

Table 1
Shows an Overview of the Expected Power Characteristics, Polarization's, Frequency Characteristics, Occurrence's for Each of the Presented Science Case

Science case	Type[—]	PFD [W/m ² /Hz]		Relative to galactic background [dB]	Dominant stokes parameter[—]	Time window of the phenomenon	Duration of emission	Occurrences [—]	Frequency range	Instantaneous bandwidth	Required resolution	Required time resolution
		Min	Max									
Solar Burst	Burst	NA	$4 \cdot 10^{15}$	43	Linear & Circular	days	s	1 to 20 per day	0.08–80 MHz	80 MHz	100 kHz	1 s
RFI (Earth)	Continuous	$2 \cdot 10^{17}$	$4 \cdot 10^{15}$	40	Linear & Circular	Always	ms	Always	0.08–80 MHz	1–10s kHz	1 kHz	1 s
Galactic background	Continuous	$7 \cdot 10^{20}$	$2 \cdot 10^{19}$	0	Unknown	Always	Always	Always	0.08–80 MHz	80 MHz	100 kHz	None
QTN (Quasi Thermal Noise)	Interference	$1 \cdot 10^{22}$	$1 \cdot 10^{18}$	7	None	Always	5 min variation	Always	0.08–1 MHz	N/A	10 kHz	5 min
AKR (Earth, day)	Burst	NA	$1 \cdot 10^{20}$	–13	Circular	hours	s	Daily	0.05–0.8 MHz	1–10s kHz	10 kHz	10 s
AKR (Earth, night)	Burst	NA	$1 \cdot 10^{15}$	37	Circular	hours	s	Daily	0.05–0.8 MHz	1–10s kHz	10 kHz	10 s
Lightning (Earth)	Burst	NA	$1 \cdot 10^{16}$	27	Elliptic	min to hour	μ s to ms	30 per s	1–100 kHz and 1–40 MHz	40 MHz	1 kHz	1 ms
Solar system planetary emissions	Burst	$1 \cdot 10^{23}$	$7 \cdot 10^{20}$	–5	Circular	min to hour	ms	Daily	0.03–40 MHz and 60–120 kHz	0.03–40 MHz	broadband and narrowband emissions resp.	1 ms - 10 s
Dark ages and cosmic dawn	Continuous	$2 \cdot 10^{25}$	$2 \cdot 10^{23}$	–40	None	Always	Always	Always	0.08–80 MHz	N/A	MHz	None
Bright radio transients from outside solar system	Burst	NA	$1 \cdot 10^{20}$	–60	None	ms to mins	ms	Daily	0.08–80 MHz	Unknown	kHz	10 ms - 1 s

Note. Derived from works of Jester and Falcke (2009); Ceconi et al. (2012); Zarka et al. (2012); Klein Wolt et al. (2012); Boujdada et al. (2013); Zarka et al. (2018); Jácóme et al. (2022); Desch and Rucker (1983); Kurth et al. (2005); Zarka et al. (1996); Kaiser et al. (1996); R. Manning and Dulk (2001); Novaco and Brown (1978); G. A. Dulk et al. (2001); Zarka et al. (2004); A. Vecchio et al. (2021); Meyer-Vernet (1979).

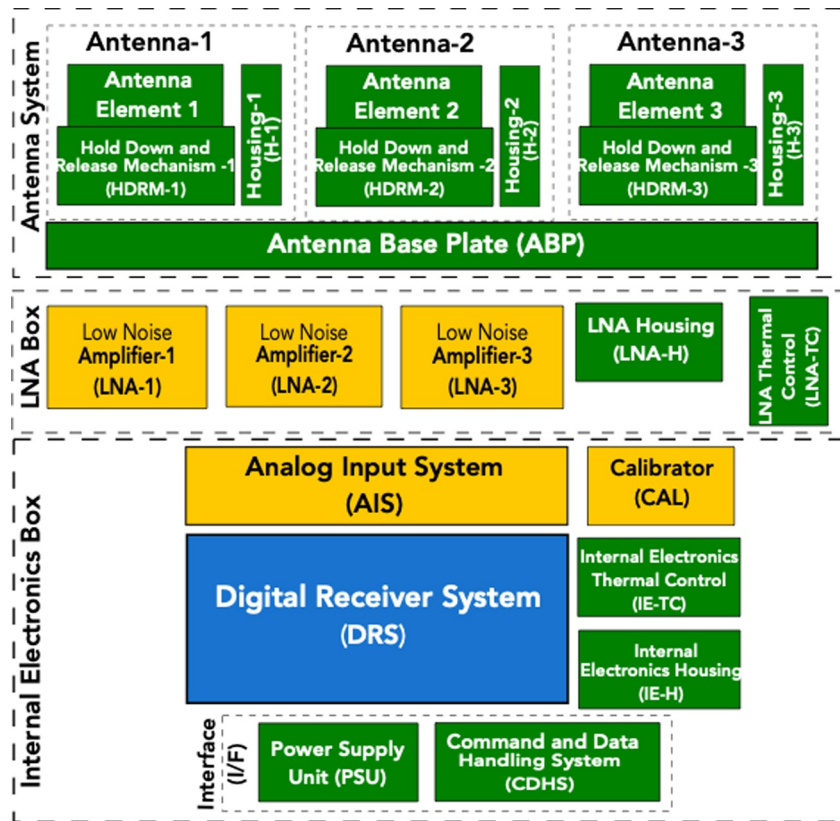


Figure 4. This figure shows the block representation of the major components of NCLE subsystem. Different colors represent the respective contributions from the various institutes in the consortium (green, ISISpace; yellow, Astron; blue, Radboud Radio Lab). [Adapted from source: Hernandez et al. (2019)].

specified lower frequencies, and with extrapolation, the uncertainties are transferred further at other frequencies. NCLE shall undertake observations at low frequencies in the 1–80 MHz range, which will be used to generate radio sky maps and overcome the limitations of extrapolated sky maps. As a technology demonstrator, NCLE will systematically tackle the instrumental and technical prerequisites essential for attaining the necessary sensitivity and resolution to observe these science phenomena consistently over an extended duration. The importance of the knowledge gained from NCLE gains further significance when viewed from a statistical perspective, particularly within the framework of future Moon-based interferometry (L. Koopmans et al., 2019; L. V. E. Koopmans et al., 2021).

3. Instrument Design

The main blocks of NCLE are the Antenna System that houses the electric field sensors (antennas), the antenna deployment system, and the Antenna Base Plate (ABP). The Low Noise Amplifier (LNA) box contains three LNA channels and the LNA thermal control unit. The internal Electronics BOX (EBOX) houses the Analog Input Stage (AIS), the Digital Receiver System (DRS), the calibrator, and a stacked assembly composed of a Power Supply Unit (PSU), Thermal Control unit (TCU), and Command and Data Handling System (CDHS). Figure 4 shows an overview of these subsystems present in NCLE. The electric field sensor comprises three deployable 5 m monopole antenna elements. The signal from the antenna passes through the Radio Frequency (RF) chain, which consists of low-noise amplifiers (LNAs) and an analog input stage (AIS). The primary function of the AIS is to condition the RF signal for sampling with an Analog Digital Converter (ADC) and to select between the first and second Nyquist sampling zones. The signal then arrives at the DRS and is sampled into the digital domain, starting with an ADC followed by digital band selection, averaging, time series capture, correlation, and storage. The electronics stack in the EBOX monitors and controls each subsystem's power, carries out internal communication, performs health checks, thermal control, and command and data handling. The electronics stack also

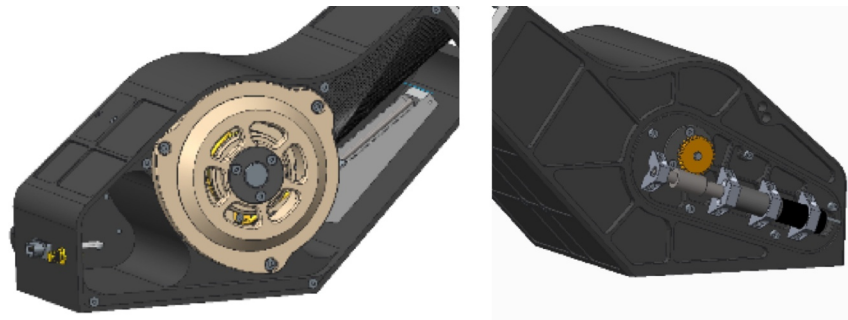


Figure 5. Antenna Housing various elements, [left] Antenna rolling element, [right] antenna deployment drive motor.

communicates with the spacecraft, manages all forms of data in and out of NCLE, carries out commands sent from Earth, and prepares data for transmission to Earth. The design of these subsystems is described in detail in the following sections.

NCLE receiver sensitivity in three different analog modes within its operating frequency range is highlighted in Figure 3. The instrument's sensitivity requirement (represented by a blue line) is derived from our scientific objectives; the QTN constrains the slope below 1 MHz, and the Galactic background radiation constrains the flat spectrum above 1 MHz. Three different analog filter settings are designed to fit the sensitivity requirement, one below 3 MHz (orange line), the second the main science frequency range from 1 to 60 MHz (green line), and the third are from the 2nd Nyquist sampling of the Analog channel, and that covers 60–80 MHz (pink line). To effectively address the dominant signal power from sources such as AKR in the lower frequency range and from the instrument itself, it is imperative to employ a dedicated 3 MHz low pass filter. At lower frequencies below 1 MHz, the system noise is system temperature dependent, and to study the effects of temperature on system performance, the 3 MHz band can provide additional advantages; this band also caters to the technical objectives, and this band shall be used to measure the QTN, Earth-AKR and also for RFI characterization. The NCLE main science band is from 1 to 60 MHz, and the design for this band is derived from the scientific objectives (see Figure 2); this band shall be used to measure the Galactic background radiation, planetary sciences (Jupiter's and Saturn's emission) and to obtain low-frequency sky map. Increasing the integration time will let us reach the required sensitivity requirement set for the NCLE main science band (1–60 MHz).

3.1. Antenna Subsystem

The electrical antenna subsystem is responsible for coupling the radio or electrostatic signal of interest, achieved with three monopole antennas. Each antenna is 5.0 m long and is composed of 0.19 mm thick high strength Carbon Fibre Reinforced Plastic (CFRP) with a cross-section diameter of 47 mm. The antenna is rolled up inside a $285 \times 140 \times 163$ mm (lxbxh) housing. This antenna housing is mounted on an antenna base plate (ABP), and the ABP is mounted on the outer side of the spacecraft. The ABP is the single mechanical interface with the spacecraft. This antenna housing is shown in Figure 5; it consists of the rolling antenna element, the motor, the deployment indicator, a drive train, and the protective covering. The primary function of the housing is to protect the antenna during launch conditions and provide the required thermal environment for the antenna in a stowed configuration. During the deployment, the monopole antenna housing lid is pushed open, and the antenna is deployed up to 5 m using the motor.

NCLE antennas are not positioned precisely orthogonal to one another due to the presence of the parabolic reflector (communication antenna of the relay satellite). For strong radio point sources in the sky, the orthogonal-like configuration of NCLE antennas makes it possible to find the arrival direction of the flux. The projected angle between each antenna is $\beta = 120^\circ$. Considering a plane intersecting any pair of antennas, the two antennas in that plane are separated by an angle $\alpha = 75^\circ$.

The basic concept for deployment of each antenna involves a drum (on which the antenna is rolled up) driven by a geared motor. The axes of the drum and the motor are perpendicular and are mechanically coupled by a worm gear. Based on our trade-off analysis between various motor types, the Brushless DC motor (BLDC) was chosen

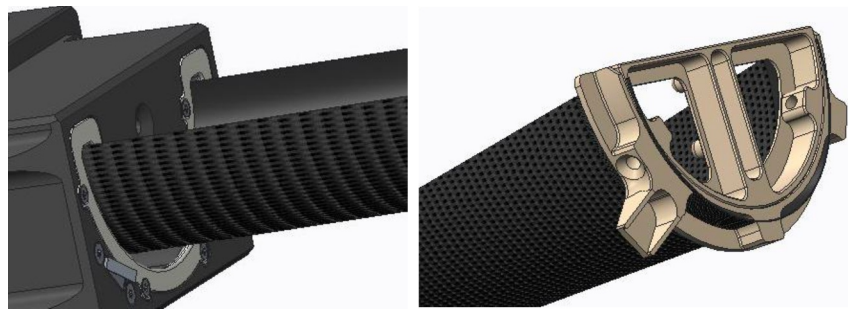


Figure 6. Antenna Housing various elements, [left] the high strength carbon fiber antenna element and [right] lightweight end stop.

as the motor; however, the BLDC motors rely on hall sensor electronics as feedback for detecting the rotor position and measuring the speed. The hall sensors with BLDC have an operating temperature range of -40° to 150° ; this limits their usage in the extreme temperature range expected at the outer part of the satellites in space. Specifically, the deployment is to be made in sunny conditions. The team had prior experience with BLDC motors and had developed an alternative method that relies on the back electromotive force (or back-EMF) to perform commutation. The BLDC motor has good space reliability, and the number of Commercial off-the-shelf (COTS) units available is high; consequentially, sensorless commutation was chosen. The BLDC motor activates the drive train that slowly unrolls the antenna element. The tip of the antenna element has a lightweight half-U-shaped end stop mounted (see Figure 6). This end stop pushes away the protective covering placed during the deployment and, when fully deployed, helps retain the antenna's half-U shape.

When fully deployed in space, the 5 m long antennas can undergo rotational inertial deflection during spacecraft maneuvers. The forces expected in flight were simulated on the full-length antenna during the buckling test. The test results showed that the antenna deflection is within the acceptance angle of deflection and does not physically impact any spacecraft equipment. During this test, it was concluded that the antenna could move freely within a cone of half-angle of 25° . Table 2 describes the antenna structural analysis outcome. The first natural frequency of the antenna is 1.0 Hz with a tolerance of $\pm 1.8\%$ for a fully deployed 5 m antenna. With a static load of $0.072 \text{ [rad/sec}^2\text{]}$ acceleration applied in 3 axes at the same time on the antenna, the tip of the antenna deflects maximum by 25 [mm]($\pm 11\%$). This deflection can also be described as a deflection zone with a cone of 0.6° . The buckling load factor of this antenna for the described load is 2.8 with a tolerance of $\pm 1.8\%$.

The NCLE LNA design was adapted from the LESIA wide-band LNA that has an operational upper band of 40 MHz (receiver used in Solar orbiter missions (M. Maksimovic et al., 2020)). The NCLE LNA cf. [5] is just as the LESIA LNA roughly sky noise limited in the range 1–20 MHz. Figure 3 in ref [5] shows that for a 5 m monopole the resonance is at 20 MHz as is the case for the LESIA simulation in the paper add details from Albert-Jan. In the “Phase-A” study of instrument development, to derive the isotropic noise flux density equations, the sensitivity of an uncoupled antenna and LNA subsystem comprising the single-ended Lesia LNA is solved in both a commercial software package (Keysight Advanced Design System - ADS) and modeled with MATLAB to verify and validate the analysis. Figure 7 presents the calculated noise flux density for antenna lengths varying from 2 to 5 m; the achieved receiver noise flux density remains above the required value for more than half of the desired frequency band. The receiver sensitivity requirement led to the selection of an antenna length of 5 m, as shorter lengths resulted in increased receiver noise, particularly noticeable at frequencies below 10 MHz. Additionally, at 20 MHz, the polarimetric behavior showed irregularities as a function of frequency. A detailed NCLE antenna design considerations analysis can be found in (Arts et al., 2019).

Table 2
Antenna Structural Analysis Outcome

Cross section diameter	thickness	Buckling Load Factor [BLF]	First Natural frequency	present zone
47 [mm]	0.19 [mm]	2.8 ($\pm 17\%$)	1.0 [Hz] ($\pm 1.8\%$)	3°

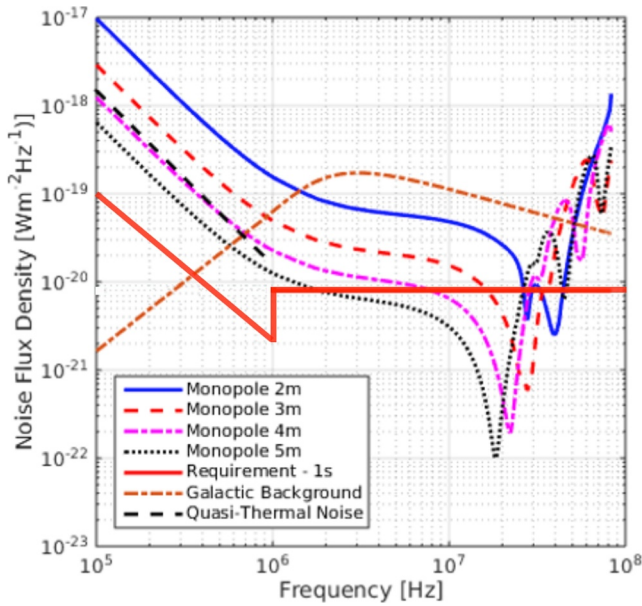


Figure 7. Isotropic noise flux density calculated for various lengths of monopole antenna connected to a differential LNA. The quasi-thermal noise is calculated for a 5 m antenna. Over most of the frequency band, the receiver noise flux density is seen to be below both the quasi-thermal and galactic background noise, only exceeding the galactic background noise for frequencies higher than 50 MHz (adapted from Figure 5 of Arts et al. (2019)).

3.2. LNA/AIS/Calibrator

3.2.1. Low Noise Amplifier

The LNA box contains three identical Low-Noise Amplifiers and an LNA thermal control (LNA-TC) unit. The LNA-TC measures and controls the temperature within the LNA box. Figure 8 shows one of the RF (LNA) channels. The RF signal enters the RF chain via a Sub-Miniature version A (SMA) connector. The impedance ratio of the antenna seen by the RF circuitry is lowered using a 4:1 coupling transformer that lowers the amplitude of the input signal. The following section in the RF chain is a 20 dB coupler used to couple the RF calibration signal into the RF system with very low insertion loss for the antenna signal and 20 dB attenuation for the calibration signal. The following is an attenuator section, and this is placed in series to lower Electromagnetic Compatibility (EMC) input levels and mitigate the risk of a non-linear RF chain. If the attenuator is turned on, the Noise Figure (NF) will increase by the same amount of the attenuation loss in dB. The low pass filter is designed based on a seventh-order Pi-type Chebychev topology, and the 1 MHz high pass filter is based on the ninth-order Chebychev. The fully differential Operational Amplifier (OPAMP) can handle strong input signals while maintaining low intermodulation products. This is achieved using a radiation-hardened COTS version THS4511-SP for band 1, with a Power Supply Rejection Ratio (PSRR) and Common-Mode Rejection Ratio (CMRR) more than 90 dB, with a gain of 17 dB. For Bands 2 and 3, this is achieved using AD8001AQ, with a PSRR and CMRR of this device being more than 50 dB and a gain of 23 dB. The dynamic range (DR) of the active LNA is 38.52 dB, with lower output third-order intercept point harmonic (OIP3L) at 18.5 dB, higher output third-order intercept point harmonic (OIP3H) at 18.7 dB and Input-referred 1 dB compression point (P1dB) at -20.02 dB.

The analog chain architecture is split into frequency bands (see Table 3) to lower the amplifiers EMC input voltages to manageable levels. The bands are: Band-1 (80 kHz–3.0 MHz), Band-2 (1–60 MHz), Band-3 (10–60 MHz) and Band-4 (60–80 MHz). Band 1 is the noisiest band due to the high power density of the EMC levels entering system. A separate low-frequency section has been implemented (blue signal path Figure 8). The input signal power level is broadband; an 80 kHz high pass filter and a 3 MHz low pass filter are implemented before the operational amplifier to limit it. The 0 dB attenuator PADs are implemented in the chain in case of return loss issues. Band-2 (1 MHz-High pass analog filter) is covered by the high side section (green signal path Figure 8). A relay switches between Band-1 and Band-2 or 3 at the input and output. For Band-2, a high order 1 MHz high pass filter attenuates the frequency below 1 MHz before the amplifier. Band-3 (10 MHz-High pass analog filter) filter is added to attenuate frequencies below 10 MHz (orange signal path Figure 8). For Bands 2 and 3, the upper-frequency cut-off is done by the Analog Input Stage (AIS) Low Pass Filter (LPF) at 60 MHz; thus, Band-2 is (1–60 MHz), and Band-3 is (10–60 MHz). Band-4 (60–80 MHz) not shown in the Figure 8, as it is implemented

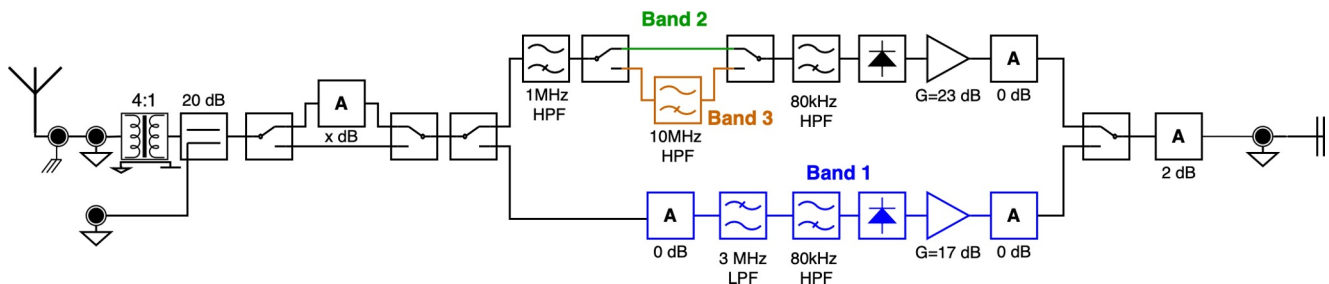


Figure 8. LNA RF channel block diagram and the signal path active during sub frequency band selection. (Band-1 in blue, Band-2 in green, and Band 3 in orange) [similar to block diagram, Figure 7 of Prinsloo et al. (2018)].

Table 3
Frequency Bands of the NCLE Receiver

Frequency band	Frequency Range
Band 1	80.0 kHz–3.0 MHz
Band 2 (main)	1.0–60.0 MHz
Band 3	10.0–60.0 MHz
Band 4	60.0–80.0 MHz

on the AIS board, where a different filter is selected to use the second Nyquist zone of the ADC in combination with Band-2. The 2 dB pad at the output creates a DC path to the ground and improves the output return loss.

3.2.2. Analog Input Stage

The AIS subsystem conditions the RF signal for sampling with the ADC. It selects the Nyquist zone and amplifies the RF input signal. The AIS system architecture is designed for receiver sampling at 120 Mega Samples per Second (MSPS). In order to sample the entire frequency range of 80 kHz to

80 MHz, the AIS enables the selection of either the first or second Nyquist zones through the use of two filters. One is a 60 MHz LPF, and the second is the 60–80 MHz Band Pass Filter (BPF). The AIS has three identical RF channels; Figure 9 shows one of the AIS channels. The AIS board is realized using the AD8001ARZ by analog devices. The AIS RF chain starts with a transformer to suppress the common-mode signals induced along the analog signal path with respect to analog ground at the LNA and AIS board interface. A low-gain amplifier is selected to ensure high linearity and reduce noise. The operational amplifier has an operating temperature range of -40 to 85°C . The amplifier stage has an operating frequency range of 80 kHz- 80 MHz with a gain of 4 dB, with OIP3 of 33 dBm and NF of 20.8 dB. The 60 MHz low pass filter has a ninth-order Cauer-Chebyshev topology. Following the amplification stage, a programmable stepped attenuator can set the analog signal level to ensure that the analog signal is within the input range of the ADC. This attenuator has an operating frequency range of 80 kHz- 80 MHz, and the attenuator of each channel can be changed to 1, 2, 4, 8 or 16 dB attenuation levels to match the output power of all three RF channels. In addition, it can be used to match the power levels between the three channels and compensate for the gain loss due to changes in temperature over time. An industry standard for efficient signal transfer is to minimize signal reflection and maximize power transfer by designing source and load impedances to be matched. The matching is called $50\ \Omega$ impedance matching. The NF of AIS at matched $50\ \Omega$ impedance is less than 16 dB. The NF gives us the degradation of the signal-to-noise ratio due to various components in the system. The lower the NF achieved, the better the performance of the system. The NF of the analog stage of NCLE is presented in the following Section 3.2.2.3.

A critical part of the AIS is the selection of the appropriate Nyquist zone required for observation (see Figure 9). Finally, the analog signal passes through another transformer at the output of the AIS board to suppress any common-mode signals that could be induced within the AIS board signal path. The plots in Figure 10 are the pass-band gains for an input signal of 0 dBm (one channel per antenna). The gain comparison between the three analog channels presented for the filter selection LPF and BPF shows that the pass-band response of all three channels is nearly identical. The out-of-band rejection for both the filter bands is better than 35 dB over a frequency bandwidth from 100 kHz up to 1 GHz.

3.2.2.1. 60 MHz Low-Pass Filter

The 60 MHz LPF on the AIS Board limits the bandwidth of the signal that the Analog Digital Converter (ADC) has to process and suppresses the clock signal of the ADC. Therefore, the cut-off slope at 60 MHz has to be quite steep. Design goals are to attenuate signals at 60 MHz by 40 dB and keep signals above 80 MHz approximately 70 dB down with a design impedance of $50\ \Omega$. The design goal is achieved with a 9th order

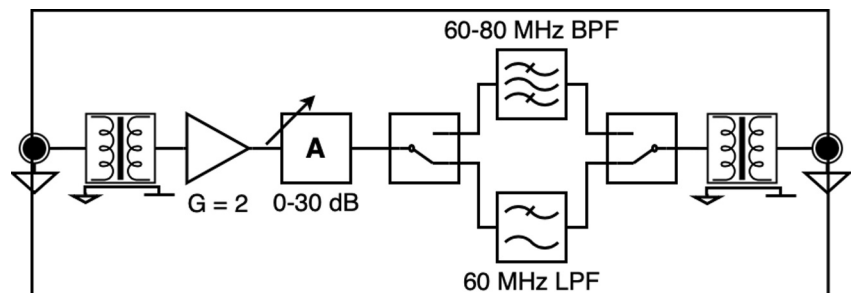


Figure 9. AIS block diagram showing a single AIS channel. The AIS attenuator is used to match the output powers of the RF input channel, and AIS provides filter selection between the first and second Nyquist zones.

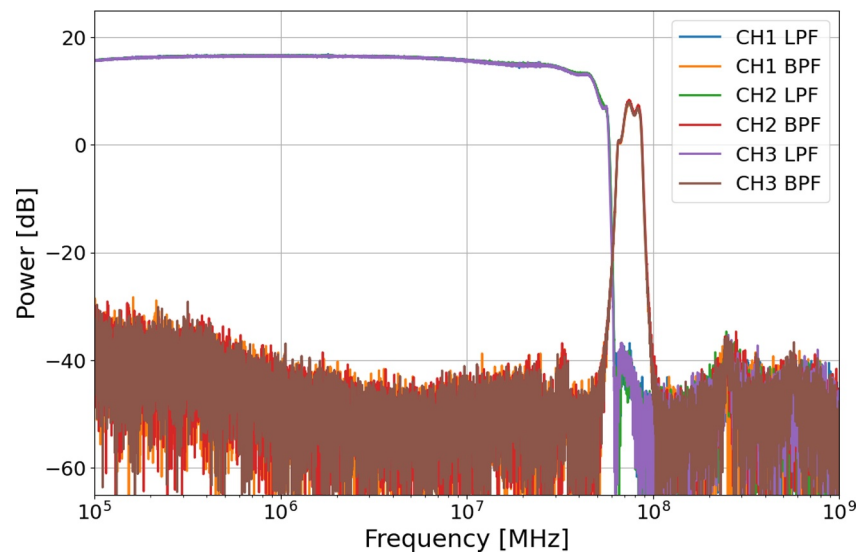


Figure 10. Pass-band gain of the three AIS channels obtained by an input signal of 0 dBm for both the LPF and BPF filters.

Cauer-Chebyshev filter. The simulated and measured performance parameters of the LPF are shown in Figures 11 and 12. The S-parameter describes the ratio of injected input to output power in an electrical system. The plot of Figure 11 shows the S21 s-parameter and provides the system's forward transmission coefficient (signal transmission from input port 1 to output port 2). The forward transmission S21 has to be close to 0 dB in the frequency of interest, which means the input signal is transmitted to the output with very few losses. The measured S21 of the LPF is close to 0 dB. The plot of Figure 12 shows the S11 s-parameter, and it provides the reflection coefficient of the system (input signal at port one and the reflection of this input signal as seen at port one). The smaller the reflection coefficient at the frequency of interest, the better the system's performance. The measured LPF reflected signal at the frequency of interest is -10 dB below the input signal. Furthermore, from the input reflection coefficient, it is clear that the filter is well matched at 50Ω up to the 3 dB cut-off frequency at approximately 52 MHz, above which the input signal is gradually attenuated, and above 60 MHz the input signal is completely attenuated.

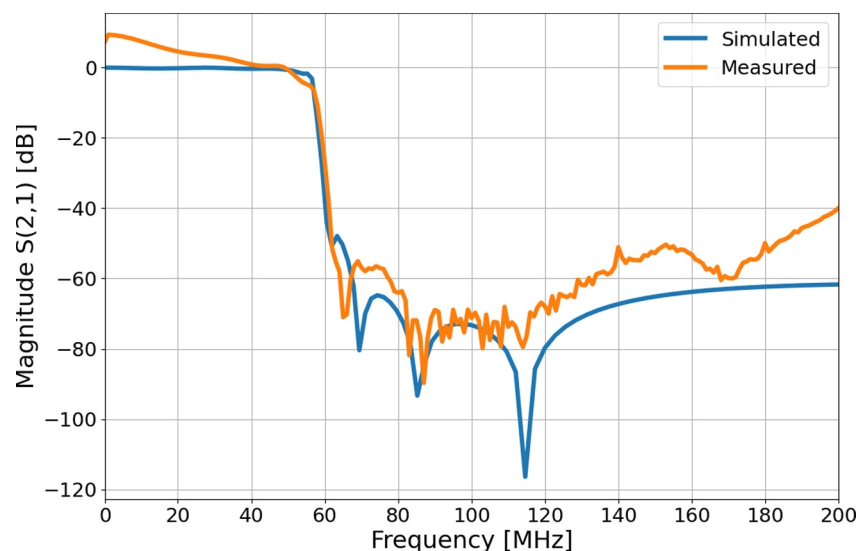


Figure 11. S21- Simulated and measured Transmission coefficient of the 60 MHz low-pass filter.

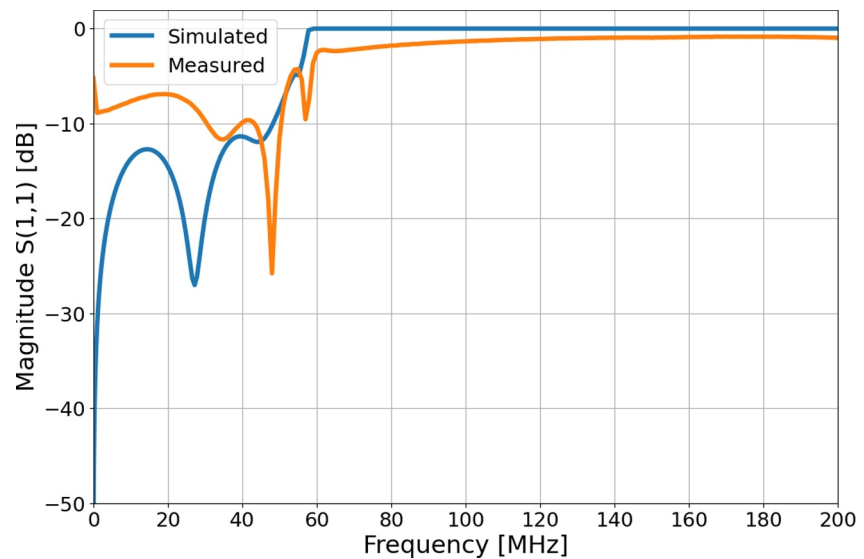


Figure 12. S11- Simulated and measured input reflection coefficient of the 60 MHz low-pass filter.

3.2.2.2. 60–80 MHz Band-Pass Filter

The 60–80 MHz BPF on the AIS board uses the second Nyquist zone. The BPF had similar design goals to the LPF. The aim was to attenuate signals at 60 and 80 MHz by 40 dB and further attenuate the signals at 40 and 100 MHz by 60 dB with a design impedance of 50 Ω . The design goal was achieved, and a steep cut-off slope was obtained at the BPF lower (60 MHz) and upper (80 MHz) cut-off frequencies. The S21 transmission coefficient of the band-pass filter is shown in the plot of Figure 13. The plot of Figure 14 shows the S11 s-parameter. The BPF reflected signal at the frequency of interest is -5 dB below the input signal.

The AIS system provides different analog configurations. Filter response can be set to LPF or BPF. The AIS provides a variable attenuation selection between 0 and 16 dB in steps of 2^n . This variable attenuation can be adjusted to the required levels and avoid detector saturation when observations are performed for longer integration times. The filter response with variable attenuation for the Low Pass Filter (0–60 MHz) is shown in the plot of Figure 15 and for the Band Pass Filter (60–80 MHz) is shown in the plot of Figure 16.

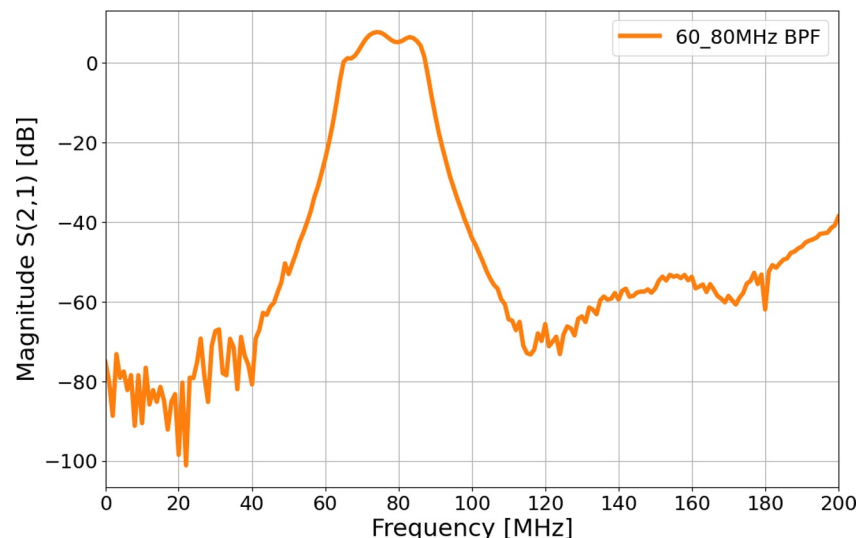


Figure 13. The Band Pass Filter response for 60–80 MHz. S11 transmission coefficient, the response attenuates by 40 dB at 60 and 80 MHz and attenuation by 60 dB at 40 and 100 MHz with a design impedance of 50 Ω .

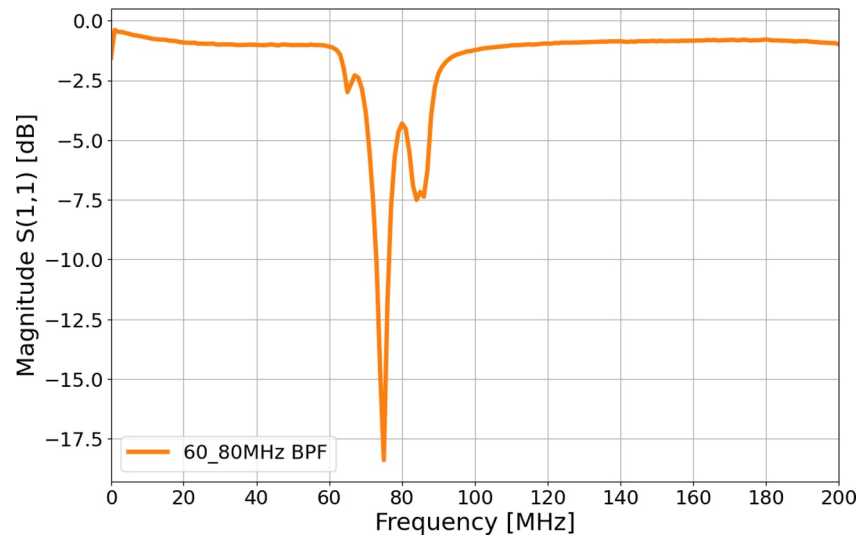


Figure 14. The Band Pass Filter response for 60–80 MHz. S11 input reflection coefficient.

3.2.2.3. AIS performance and Noise Figure

The plot of Figure 17 shows the AIS board assessment by comparing the simulated and measured S-parameters for the forward transfer co-efficient. The three solid curves show the measured pass-band forward transmission coefficient of all three analog channels (CH0 – CH2). It is noted that the measured responses of channels 1 and 2 are nearly identical, and compared with the simulated curve (Sim No T-PAD), both channels operate as expected, with a slight deviation from the simulated response at the higher end of the band. Considering the variation in pass-band gain, it is seen that the gain of channels 1 and 2 vary by ≈ 2 dB. In order to reduce this gain variation, a 3 dB T-PAD network is inserted after the amplifier in channel 0. As expected, this results in a 3 dB reduction in gain, seen in both the simulated and measured response, and reduces the gain variation to within 0.6 dB over the pass-band. Finally, the 3 dB cut-off frequency of the pass-band is measured at 55 MHz.

The plot of Figure 18 shows the measured channel crosstalk between the three analog channels. The isolation is better than 40 dB across the entire frequency band, with the isolation between adjacent channels nearly identical. Isolation between adjacent channels increases toward the higher frequency of the operating band. However, the filter suppression decreases the isolation after 60 MHz (the LPF cut-off frequency). Finally, the isolation between

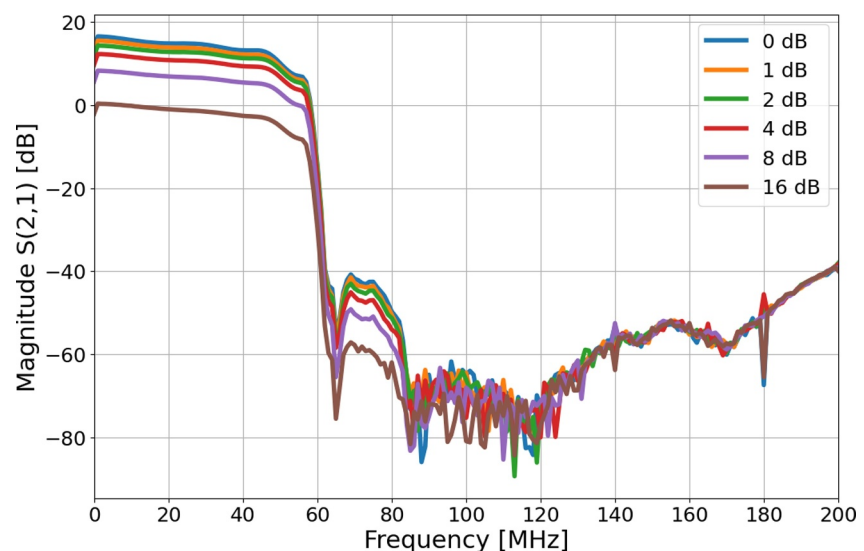


Figure 15. Filter response for variable attenuation from 0 to 16 dB in steps of 2ⁿ LPF.

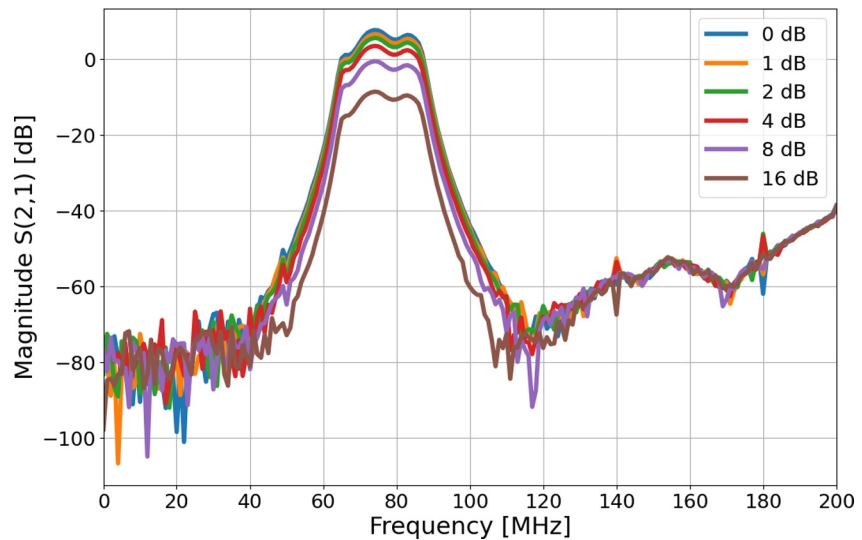


Figure 16. Filter response for variable attenuation from 0 to 16 dB in steps of 2 dB BPF with AIS using the 2nd Nyquist zone.

channels 0 and 2 is lower than adjacent channels. The plot in Figure 19 shows the forward transmission coefficient of channel 0 for the attenuator level set from 0 to 30 dB in the step of 10 dB. To better illustrate the accuracy of the attenuator settings, all curves are normalized to the same level of 0 dB attenuator setting. Comparing the response of each attenuator (10, 20, and 30 dB) settings with the nominal transmission coefficient at 0 dB. An initial 10 dB attenuation step is seen to introduce a maximum deviation of 1.2 dB is detected. However, comparing the variation in the transmission coefficient for 10, 20 and 30 dB, the attenuation level is set to within 0.5 dB accuracy with the accuracy improving to below 0.3 dB at frequencies higher than 10 MHz. A programmable step attenuator is implemented using Mini-Circuits DAT-31R5A-PP+, the deviation at the first 10 dB attenuation can be attributed to the input return loss of the attenuator at frequencies below 100 MHz. The results for the other channels are identical in performance and are not presented here. The plot of Figure 20 shows the simulated NF of an AIS channel for both LPF and BPF filter settings against the measured NF. The measured NF of the AIS channels agrees well with one another. The NF measured for the LPF is slightly higher than the simulated

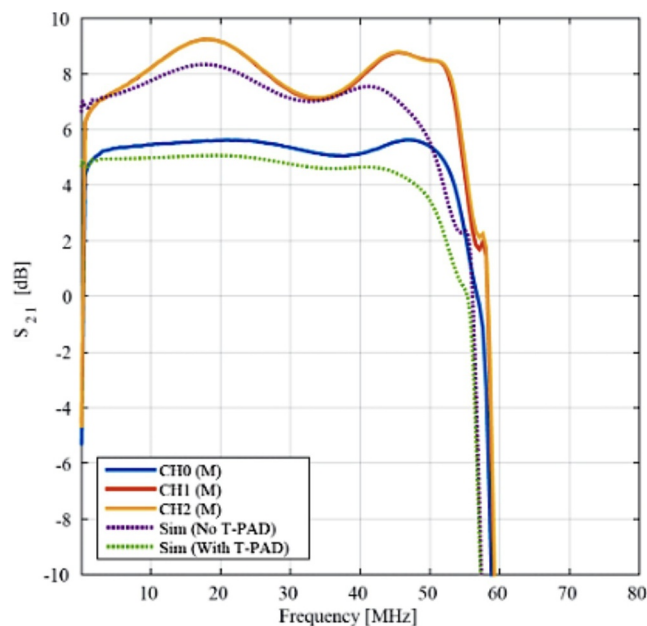


Figure 17. Measured and simulated forward transmission coefficient of the AIS board for pass-band response.

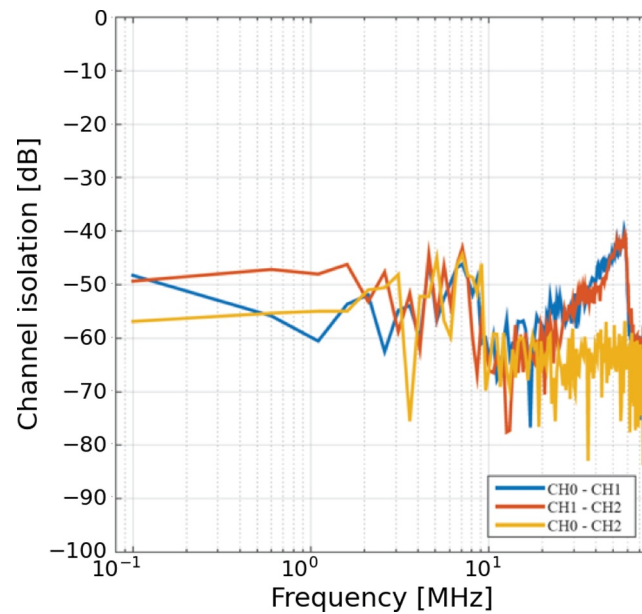


Figure 18. Measured AIS performance parameters, the channel isolation.

performance. The higher NF observed between 60 and 80 MHz is due to the additional loss as the BPF filter response is ≈ 15 dB lower than the LPF (see Figure 16).

3.2.3. Sky Noise Limited

The NCLE LNA is just like the LESIA LNA, roughly sky noise limited in the range of 1–20 MHz. Figure 3 in Prinsloo et al. (2018) shows that for a 5 m monopole, the resonance is at 20 MHz, as is the case for the LESIA and NCLE. The NCLE analog system sensitivity per band is presented. Figure 21 shows the sensitivity of the analog signal path for Band-1, and in this band, the required sensitivity level is not achieved. This is due to the input

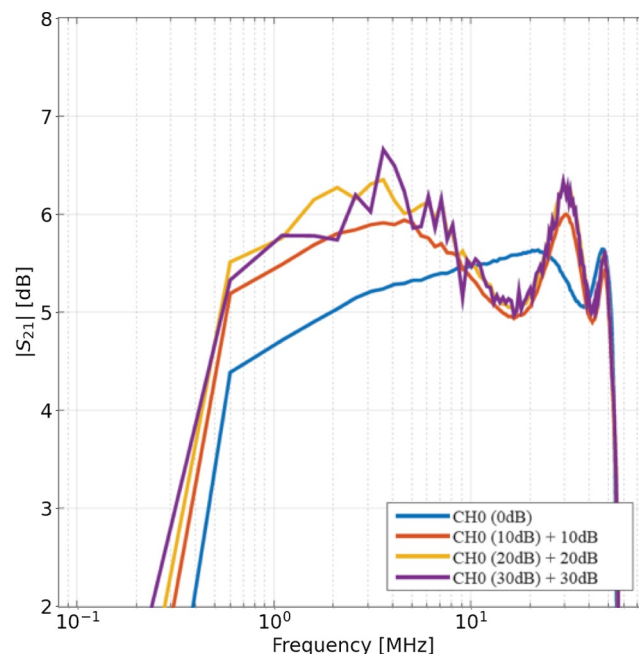


Figure 19. Measured AIS channel response for attenuator settings 0–30 dB in 10 dB steps.

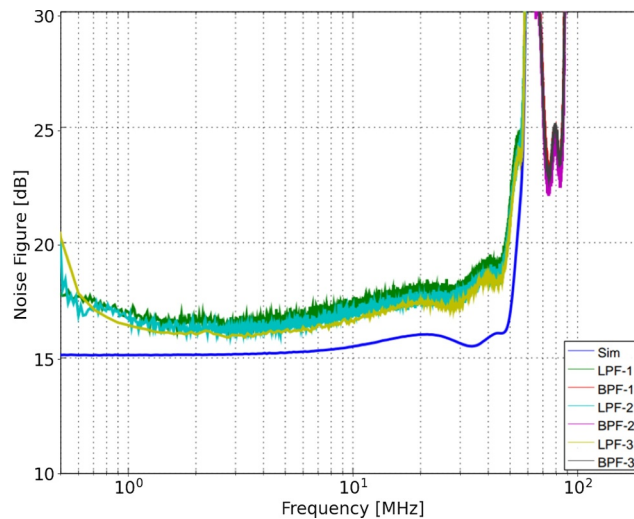


Figure 20. Simulated and measured NF of channel 0 of AIS subsystem.

transformer and the filters placed before the LNA. A further reduction in gain occurs, and this is done in order to improve linearity results. In this band, the instrument is sky-noise limited, and this LNA Band-1 design produces an output voltage within the range of the ADC for measurements. Figure 22 shows the sensitivity achieved for Band-2. The sensitivity achieved within these bands is below the sky noise for the entire frequency band and achieves the requirement for frequencies above 4 MHz. Figure 23 shows the sensitivity achieved for Band-3. The receiver sensitivity in this band satisfies the requirement for nearly the total bandwidth (10–80 MHz) and is mainly below the sky noise for the entire frequency band. In conclusion, achieving the requirements posed a partial success for the main science band. However, the other two bands presented technical challenges due to the tight development time frame of 2 years. It is worth noting that noise flux density can be improved by increasing integration time, particularly in the primary science band. However, this approach is less effective for the 3 MHz band due to system noise limitations. The initial objective to measure QTN was not realized in practice due this filter implementation. Surprisingly, in the final NCLE instrument design, the band below 3 MHz emerged as the noisiest among the three bands. The noise is attributed to the instrumental factors rather than the observed external background spectrum.

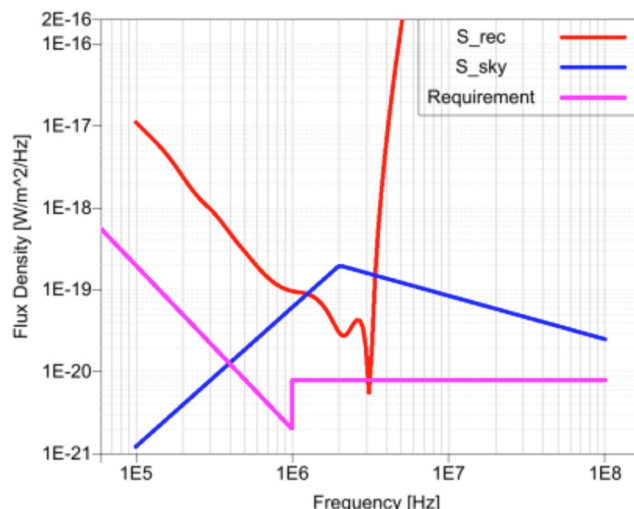


Figure 21. Measured NCLE analog receiver sensitivity for Band-1.

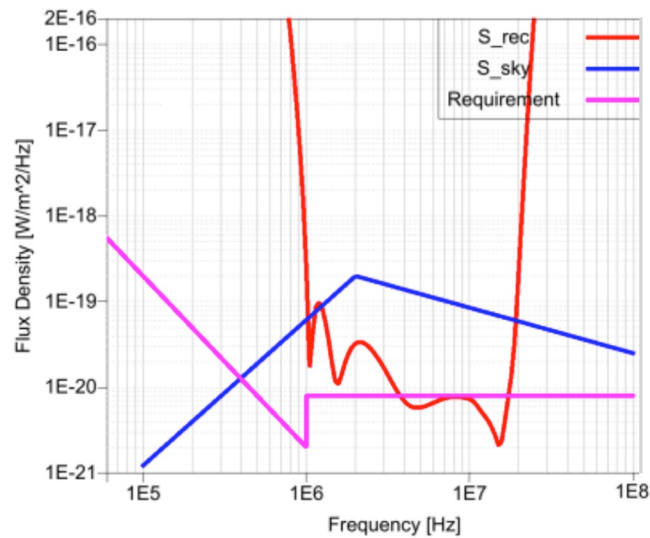


Figure 22. Measured NCLE analog receiver sensitivity for Band-2.

3.2.4. Calibrator Unit

For low frequencies ($f \leq 10$ MHz), the antenna patterns are those of standard dipoles. The patterns become more complicated for higher frequencies and are influenced by the spacecraft's structure. The absolute calibration can be done using strong astronomical point sources (Cas. A, Cyg. A, Tau. A, Vir. A), global sky model for above 10 MHz, variable point sources such as Jupiter emissions, and communication transmitter at Earth or satellites. The receiver chain consists of active and passive components whose performance can vary with temperature and aging. The impulse response of a receiver chain is the Fourier transform of its transfer function. A repetitive pulse or comb generator can be used for accurate relative pass-band calibration, both in amplitude and phase.

A frequency comb generator is used for the onboard calibration of the NCLE RF chain for relative calibration. Figure 24 shows the calibrator schematics of NCLE. The central 120 MHz Clock (OCXO) clock signal of the NCLE is converted to the sine wave or square wave with positive and negative amplitudes into a signal with a positive amplitude. The frequency divider (Hittite 87001) divides the clock signal by a factor of 100 or 1,000 (decade frequency dividers). An 80 MHz low-pass filter filters the pulses from the pulse generator, removing the

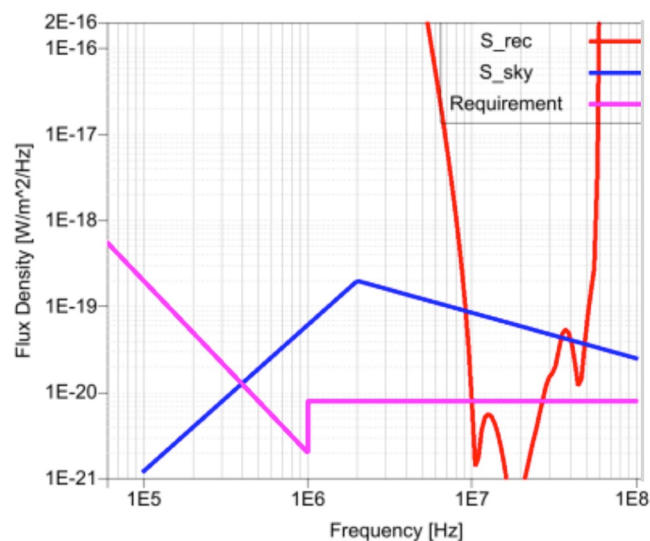


Figure 23. Measured NCLE analog receiver sensitivity for Band-3.

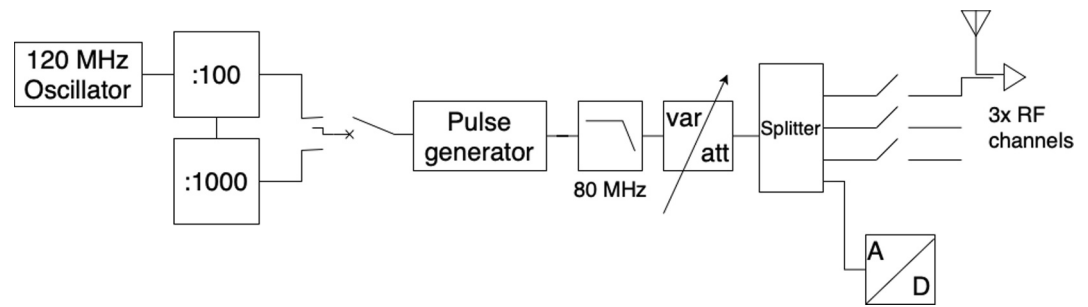


Figure 24. NCLE calibrator circuit schematics.

high-frequency components from the pulse to avoid aliasing in the ADC. A variable attenuator can attenuate the signal in steps of 0.5 dB to the desired level. The attenuated signal is split into four equal parts, fed to the three RF channels; the fourth is the direct calibration channel. The LNAs are differential, which means they amplify only the differential part of the input signal, and the differential part of the pulse signal is also input to the LNA. The performance specifications for the calibrators are RF 50 Ω , frequency range 80 kHz–200 MHz, Voltage Standing Wave Ratio (VSWR) 2:1, max pulse width 12.5 ns, pulse rate configurable 100 kHz and 1 MHz, input clock 120 MHz (form OCXO). A fifth-order Chebyshev low pass filter design is used for 80 kHz, and a tenth-order Chebyshev low pass design for an 80 MHz anti-aliasing filter.

A simulation has been performed to evaluate the calibrator's performance, and the schematic of this circuit is shown in Figure 25. A Gaussian pulse (1) is generated with a Full-Width Half Maximum (FWHM) of about 10 ns. This Gaussian signal is then passed through (2) a 5th order Chebyshev High Pass Filter (HPF) with a cut-off frequency set at 80 kHz to remove all the low-frequency components. The next stage (3) is a 10th order Chebyshev LPF with a cut-off frequency set at 80 MHz used as an antialiasing filter. The last stage is analog-to-digital conversion at 200 MSPS. Blocks 2, 3, and 4 here simulate the NCLE receiver chain. The amplitude of Fourier transforms of the Gaussian-shaped input pulse and the signal at the end of the simulation receiver chain is shown in Figure 26. It can be seen in the frequency domain that although the amplitude decreases by 5 dB at 80 MHz concerning the highest amplitude, the calibration signal can be considered to be broadband and a stable signal for calibrating the receiver chain for power gain in the operating frequency range of 80 kHz to 80 MHz.

Figure 27 shows the simulation of the calibrator pulse chain at different rates of 150 kHz (blue), 1.5 MHz (green), and 15 MHz (red). The simulations were performed at these pulse rates; however, in implementing the instrument, the pulse rates chosen are 100 kHz, 1.0 MHz, and 15 MHz. The pulse shape in all cases is independent of the pulse rate. The pulse amplitude has been measured as a function of the attenuator setting (see Figure 28). For the 1.5 MHz pulse, it can be observed that a setting with 20 dB attenuation reduces the amplitude of the output signal by a factor of 10 concerning the pulse at 10 MHz, as expected.

A pulse train in the time domain results in a comb of peaks in the frequency domain. Hence, the repetition rate of the pulse train can be measured by measuring the spectrum. In Figure 29, the output pulse signal of the calibration at a different pulse rate of 100 kHz and 1.0 MHz are shown. Due to a large number of peaks for the pulse rate of 100 kHz (orange) in Figure 29, the spectrum appears as a continuum; these peaks become visible at a closer inspection (inset picture) from 40 to 45 MHz. The measured spectra in Figure 29 also show that the power of the peaks decreases after 90 MHz. At 80 MHz, the power is 3 dB below the highest at 15 MHz.

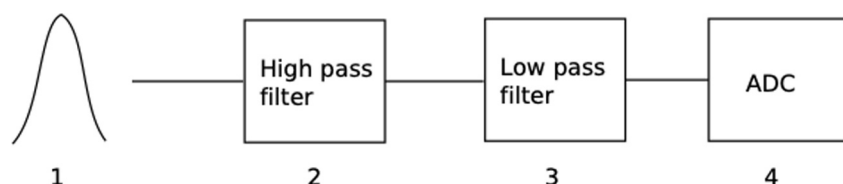


Figure 25. NCLE calibrator simulation circuit schematics, (1) Gaussian Pulse, (2) 5th order Chebyshev HPF, (3) 10th order Chebyshev LPF and (4) ADC.

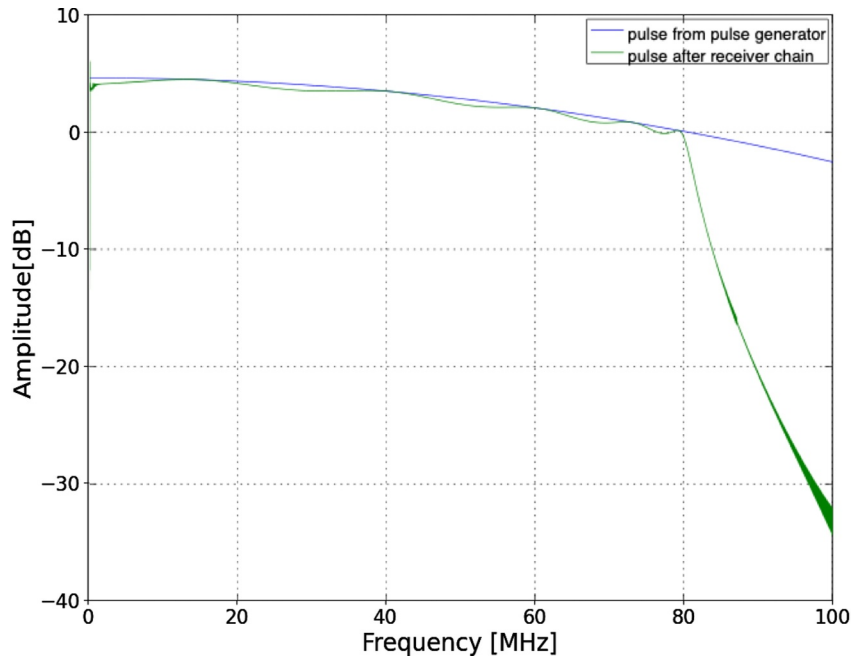


Figure 26. Amplitude of Fourier transforms of the Gaussian-shaped input pulse (blue) and the signal (green) at the end of the simulation receiver chain.

During NCLE operation, the drift over temperature will be calibrated; the calibrator signal is recorded before every long observation. As part of the ground thermal tests, the calibration system is tested in a thermal test chamber at temperatures of -40 , -10 , 20 , and 60°C . Figure 30 shows the calibrator output pulse shape at different temperatures. The pulse amplitude shows slight variations with temperature; there is no phase change. At -40°C , the amplitude is 7% higher than at room temperature (approx 0.6 dB), while at 60°C , the amplitude is about 2% lower than at room temperature (≈ 0.17 dB).

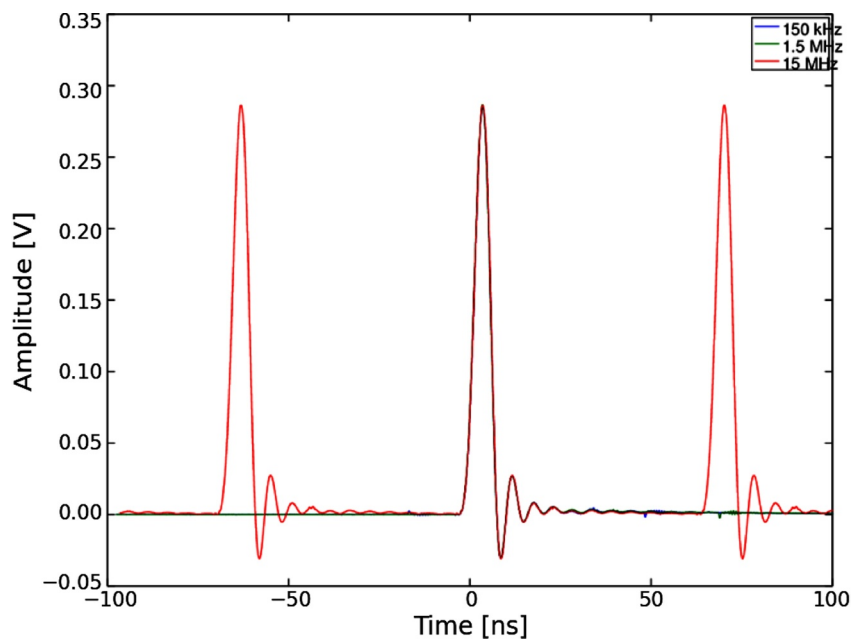


Figure 27. Pulse shapes at full amplitude for rates of 150 kHz (blue), 1.5 MHz (green), and 15 MHz (red).

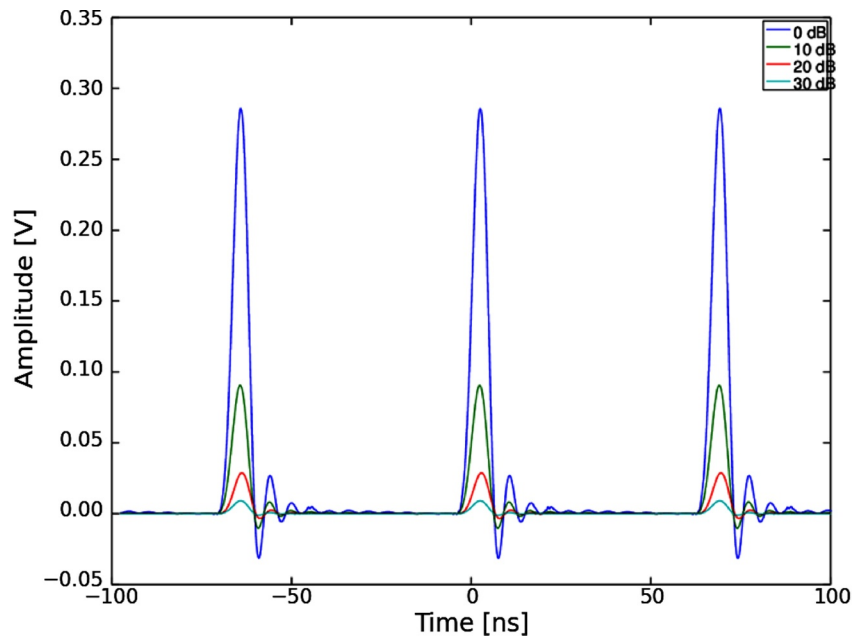


Figure 28. Pulse shape for different attenuator settings of 0 dB (blue), 10 dB (green), 20 dB (red), and 30 dB (cyan).

3.3. Clock(OCXO)

The clock stability requirements for the NCLE scientific objectives can be divided into short-term and long-term clock stability issues. The short-term clock stability relates primarily to clock jitter, which is the timing variation due to the clock signal edge deviating from the ideal position; the jitter-related effects strongly impact the overall SNR system. The long-term clock stability is more specifically tied to the VLBI observation mode. Here, clock drift must be constrained to correlate the resulting data with other instruments.

The jitters that cause issues with short-term clock stability include the internal jitter in the ADC modules (from process variation during production), the jitter incurred from interference on the clock distribution lines on the Printed Circuit Board (PCB) and cabling and the added jitter of any components that the clock signal passes

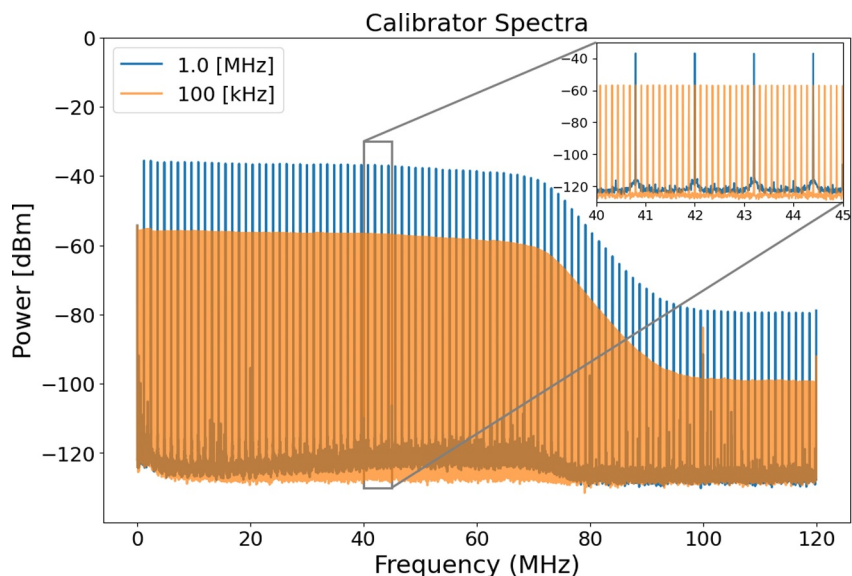


Figure 29. Spectra at the output of the pulse generator for different pulse rate rates of 100 kHz (orange) and 1.0 MHz (blue) with attenuator settings of 0 dB. (inset from 40 to 45 MHz).

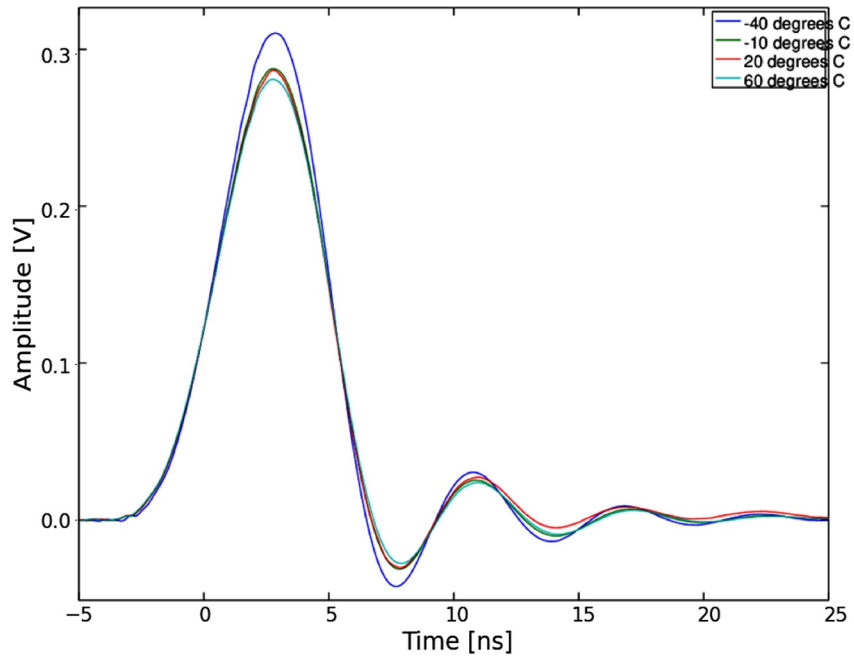


Figure 30. Pulse shape for different temperatures of -40° (blue), -10° (green), 20° (red), and 60° (cyan) with attenuator setting of 0 dB.

through such as clock distribution logic. Furthermore, it should be noted that a significant part of this noise depends on the thermal conditions and that clock stability over a more extensive temperature range should be considered. Figure 31 shows the impact of clock-jitter on SNR for different signal frequencies. For a full-bandwidth (80 MHz) signal resolution of the NCLE instrument at an Effective Number Of Bits (ENOB) of 12, a clock signal with sub 1 ps jitter is required to achieve a strong SNR >50 dB.

The long-term clock stability of the system is characterized using the Allan variance of the clock source, which measures the nominal frequency drifts over more extended periods. We must ensure that the drift is sufficiently constrained to enable correlation for the VLBI mode. The clock coherence time (the VLBI observation period) is 30 min for the NCLE science goals. During this period, a Root Mean Square (RMS) clock deviation of, at most, 1

radian can be allowed in order for the VLBI signal to correlate correctly with other sources. Figure 32 provides an overview of how several clock sources of different types perform in this regard. Considering the bandwidth of the NCLE instrument and a minimal coherence time of 30 min, the primary exciting clock sources for NCLE from this plot Figure 32 are the Airbus OCXO-F and the SA.45s. The two clocks specified are an oven-controlled crystal oscillator and a Chip Scale Atomic Clock (CSAC). However, Airbus OCXO-F is the best candidate for the NCLE instrument's bandwidth. For the NCLE instrument, a space-qualified OCXO from AXIAL (AXIOM6060A) is used, a similar clock as the Airbus OCXO-F with frequency of 120 MHz; the Allan deviation measurements for the Axtal version are shown in Figure 33, a sample at 100 MHz with AXIOM6060 A have been measured, and the jitter for this clock is smaller than one ps. The requirement was to have a clock signal with a sub one ps jitter to achieve a strong SNR >50 dB, which was achieved in NCLE using AXIOM6060A.

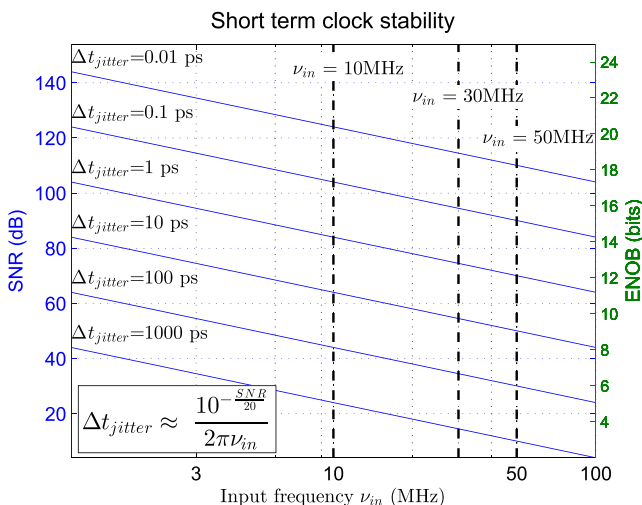


Figure 31. Clock-jitter impact on achievable SNR for different signal frequencies (source: Rajan et al., 2016).

3.4. Digital Receiver System

The analog signal that arrives at the DRS gets sampled into the digital domain, with different frequency sub-band selection, averaging, channelizing, Fast Fourier Transform (FFT), triggering, and storage of the measured spectra. For

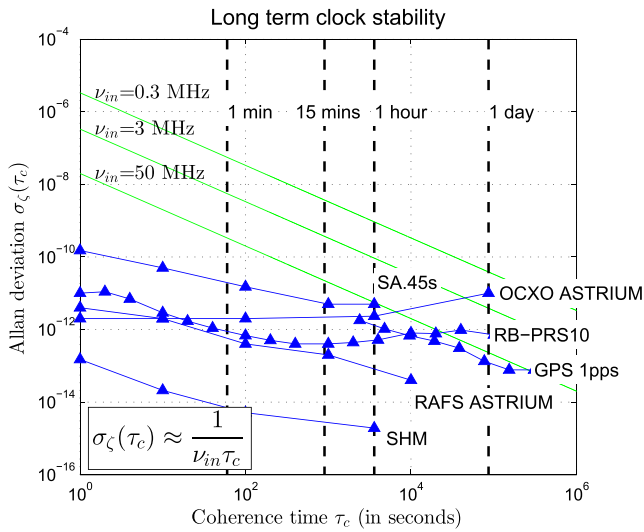


Figure 32. Coherence time for several input frequencies in seconds versus the Allan deviation of several free running clock sources (source: Rajan et al., 2016).

the hardware of the DRS, the choice was made to use COTS hardware rather than a custom-designed DRS to meet the short development phase and launch time of 2 years. The use of COTS technology in space applications is increasingly gaining traction. Despite their vulnerability to environmental factors such as radiation effects and temperature variation, the utility of COTS electronics has been well demonstrated across various scenarios. A meticulous case study of NCLE-DRS with COTS Field Programmable Gate Arrays (FPGA) was conducted (van Harten et al., 2017) that projected an acceptably low error rate for the FPGA processing. Even in severe space weather circumstances, which could lead to a significant amount of soft errors, very few are expected to be critical; however, these can be detected, and potentially, the affected data can be flagged using Code Redundancy Check (CRC). The DRS functions reliably with minimal impact on data processing and recording. This feasibility study concluded with selecting a data processing and storage module from SCS-space (<https://www.scs-space.com>) that fits the processing and storage requirements; however, it was missing an ADC. So, a four channel input with a maximum sampling rate of 125 MSPS 14-bit ADC module was designed and built using two analog devices AD9645 ADC.

Figure 34 shows a global overview of the NCLE DRS. These specifications are summarized in Table 4. The first stage is the Analog Digital converter, and the second is the COTS receiver from SCS-space. The ADC has four analog input channels (3 from the antennas and one directly from the calibrator), one clock input Channel, a 14-bit ADC resolution, and an ADC sample Rate at 120 MSPS with an RF input range of 80 kHz–80 MHz split into two bands 80 kHz–60 MHz and 60–80 MHz to satisfy the Nyquist and avoid aliasing. The independent calibrator input allows the onboard capability to gain calibration. Each analog channel gets the calibrator signal folded in the calibration mode before the LNA stage. The ADC has a maximum sampling rate of 125 MSPS samples; for NCLE operation, the ADC samples analog signals at 120 MSPS, a choice made to have a consistent sample rate. The conversion sample depth is 14 bits, of which ≈ 12 bits remain as effective bits due to internal ADC noise.

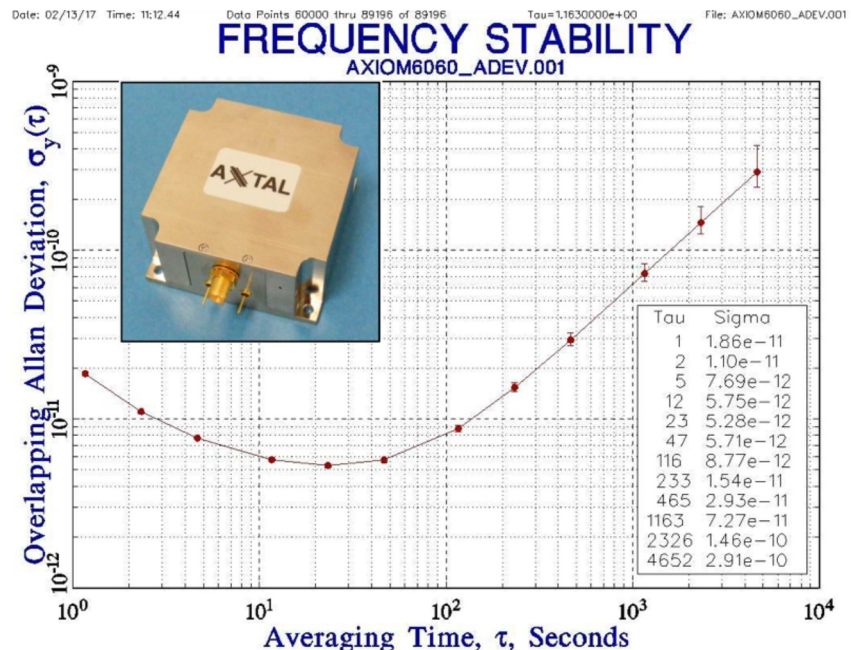


Figure 33. Allan Deviation measurements of the OXCO from Axtal versus averaging time [source:Axtal.com - AXIOM6060A].

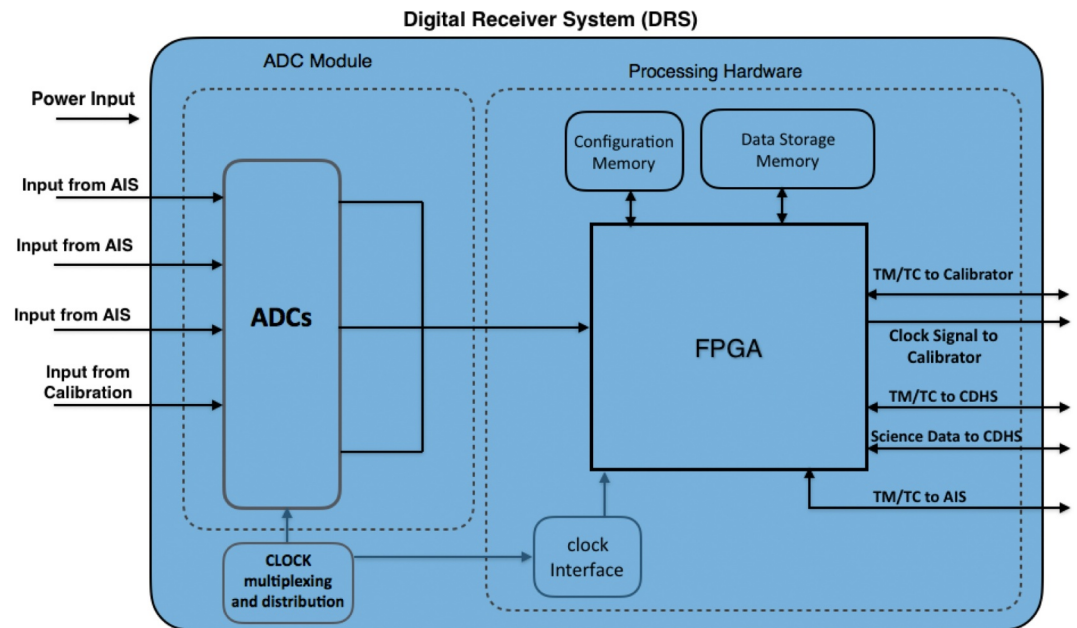


Figure 34. The NCLE Digital Receiver Subsystem's block diagram shows the hardware subsystems and interfaces.

The DRS includes a Kintex 7 FPGA (XC7K160T). The operating temperature of the receiver is between -10° and 50° and the survival temperature range is from -25° to 60° . The power supply of the SCS Receiver is a single 5V supply, with a peak power consumption of 5.4 W. The FPGA is customizable for various interface protocols, and DRS configuration is handled externally. The FPGA firmware is responsible for signal processing and control within the DRS system. In this segment, the digitized signals can be processed in several ways, depending on the active recording mode of the DRS. The DRS subsystem uses spectral recording mode, where the frequency spectrum of the incoming sampled signals is correlated and averaged. This mode's selected spectral width, resolution, and time resolution are configured from CDHS according to the scientific objective of interest. Measured spectra are stored on the onboard DRS memory, ready to be read out later. The spectral mode is the most versatile mode of NCLE, offering the chance to study numerous sources of radio emissions and making it possible to perform goniopolarimetry on the received signals. Goniopolarimetry is a technique used for direction finding of the sources; these techniques provide the direction of the wave vector, the polarization state, and the flux of the observed electromagnetic wave (Cecconi, 2014; Cecconi et al., 2008, 2009). NCLE can also operate further in three modes: Triggered, beamforming, and VLBI. The VLBI, Triggered, and beamforming modes are scheduled to be implemented with the next NCLE firmware update in space; due to the short development phase of 2 years, these modes are currently not implemented in the flight model but are under testing and development with the ground engineering model.

The spectral and cross-correlated powers of the three monopole antennas are measured through programmable time frequency windows on two antennas. The NCLE receiver measures the spectral and cross-correlated powers at all times for the (X, Z), (Y, Z), and (X, Y) pair of antenna configurations. Figure 35 shows the signal flow of the DRS system. The ADC digitizes the analog signal, and the X-bar makes the Input selection; the selected signal is filtered, and a window function is applied before spectral conversion is done by applying an FFT algorithm. The FFT output is scaled to reduce the data volume. The scaled FFT spectral output is converted to visibilities, the correlation products. These are then accumulated based on the integration time and are framed and stored, ready to be downloaded to the ground later. The individual stages of the DRS are described in this section:

X-bar stage: The input crossbar (or X-bar for short) links one of the four available input channels to one of the three available data processing channels.

Table 4
Technical Specification of NCLE DRS

Specification	ADC and SCS
Channels	4
Sample rate	120 MSPS
Band-width	80 kHz–80 MHz
Power	1 and 5.4 W
Resolution	14 bit
Crystal	40 MHz
Memory	2 Tb flash
ENOB	~12

Note. ENOB, Effective Number of Bits.

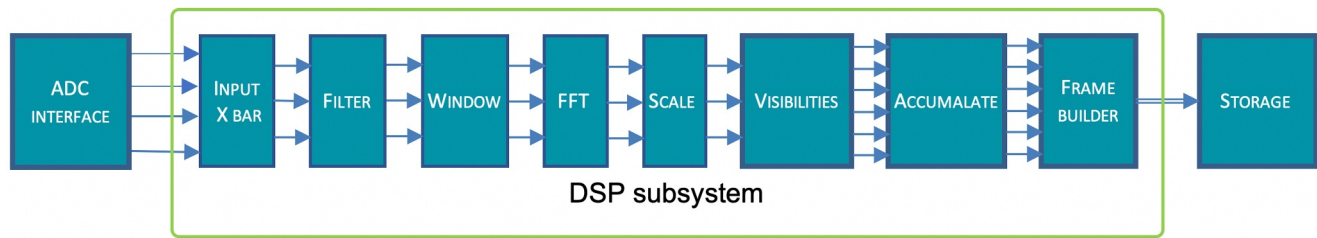


Figure 35. The DRS signal processing data path.

The X-bar selects the three inputs from three antennas in the science mode. In the calibration mode, the X-bar selects the Calibrator signal and two of the three (X, Y, Z) antenna RF Channels.

Filter stage: In this stage, the signal is filtered and, at the same time, decimated in order to reduce the sample rate. This decimation will, in turn, increase the spectral resolution of the FFT stage. The various decimation operating modes are Pass-through, 4x decimating filter, and 9x decimating filter. The pass-through mode allows the signal to pass unfiltered and unchanged. The 4x decimating filter splits the full 0–60 MHz into four equal sections of 15 MHz bandwidth and reduces the sampling rate by a factor of 4. The 9x decimating filter splits the full 0–60 MHz into nine equal bands of 6,66 MHz bandwidth, reducing the sampling rate by 9. Only one band is chosen out of 4 (or 9) for operation in either 4x (or 9x) decimation. For the second Nyquist band (60–80 MHz), decimation 4 (or 9) works similarly. With 4x decimation, two subbands 60–75 MHz and 75–90 MHz, the 9x decimation splits the band into three subbands of 6,66 MHz each. A unique band is also designed to detect the Jupiter S-Burst events from 15 to 30 MHz with a two-millisecond integration time. The 4x decimation means a 25% duty-cycle; however, the 64 frequency bins are discarded from the edges in case of 1k-FFT to fit the data into a 16k-byte DRS memory page, giving a lower duty-cycle of 21.87% (11% for decimation 9), and 24 frequency bins are discarded with 16k-FFT 24.9% (9.7% for decimation 9).

Window stage: The data can be windowed before spectral conversion to reduce the FFT stage's spectral leakage. The window can be either turned ON or OFF. When the window is OFF, the samples are multiplied by a factor of 1, so the data remains unchanged. When the window is ON the samples are multiplied by a factor determined by the Blackman-Harris window function. In this stage, 1k of 16k FFT length is used (and the configured length is used as window length for all the following stages).

FFT stage: The FFT length is configurable from 8 to 16,384 points in powers of 2. In order to prevent signal distortion due to clipping, the unscaled FFT is used. For the 16-bit input signal, the longest FFT length output required is 31-bit. The output is three complex-valued spectral outputs, each composed of a 31-bit real and 31-bit imaginary number. The inputs are the three channel, 16-bit real-valued signals.

Correlation stage (Visibilities), The (complex) spectral data is first converted into correlation products. In total, six correlation products are calculated. Three auto correlations (XX*, YY*, ZZ*) and three cross-correlations (XY*, XZ*, YZ*). The autocorrelations are, by definition, real-valued numbers representing the signal power in one channel and obtained by multiplying their complex conjugate. Cross-correlation is complex-valued numbers representing the power and phase difference between two signals. As pre-configured, the correlations are performed per frequency bin in 1k-FFT (449 bins) and 16k-FFT (8171 bins).

Accumulator stage: In this setup, a total of 9 accumulators (adders) are required, 3 for the auto-correlation and 6 for the cross-correlation (3 for the

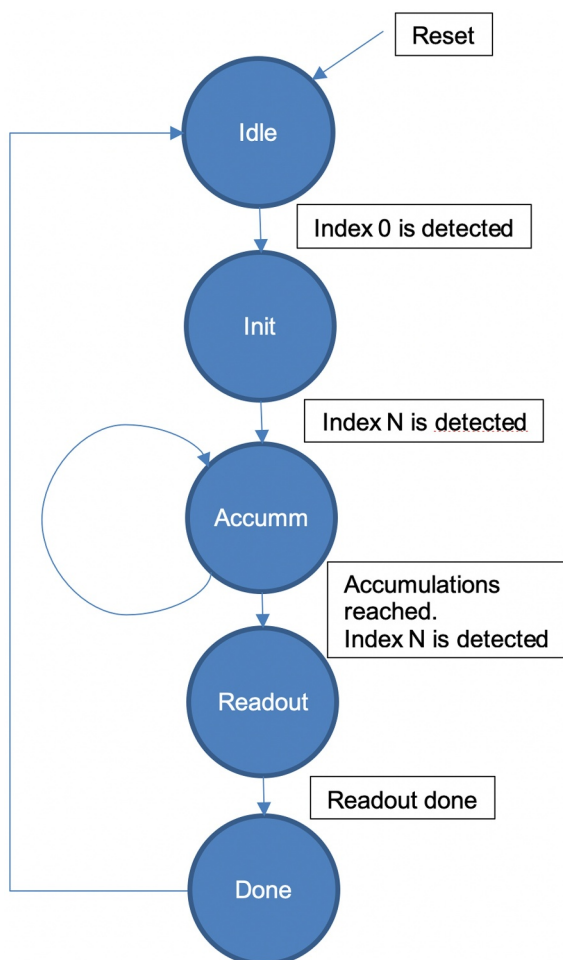


Figure 36. The DRS accumulator state diagram (Index N defines the bin size * the number of integrations).

Table 5
DRS Signal Processing Bit-Widths

DRS stage	Bit width
X-BAR	Signed 14
FILTER	Signed 16
WINDOW	Signed 16
FFT	Signed 31
FFT scaling	Signed 24
Visibilities	Signed 48
Accumulate	Signed 48
Frame builder	Float 32

real part and 3 for the imaginary part). These nine accumulators share one large RAM block to store the previous accumulation result. All accumulators share the same memory for ECC error corrections. When a new sample arrives, the previous value of that index is fetched from memory. The previous and current values are added, and the result is stored in the memory. This accumulation loop is shown in Figure 36. It is idle when the accumulator waits for a new experiment and integration to begin. When the experiment starts, it is moved to the initialization state, where the first spectrum is written to memory. The following is the accumulation state where the last written spectrum in the memory is added with the new spectra, and the sum is stored in the same memory. This addition or accumulation loop is repeated until the specified integration time. After the integration time is reached, the accumulation result is read from memory to the next stage. The accumulator is set to the final state, meaning the accumulation and readout have finished.

Frame builder stage: Meta information such as system settings, experiment settings, and timestamps are added to the experiment data. The metadata and experiment data are packed into experiment frames and stored in flash memory.

The DRS signal processing is all based on fixed point calculations. Across the signal path, several multiplications and additions are performed, so the bit width is changed at several points in the system. Table 5 lists an overview of the selected bit width. The ADC output is a 14-bit signal, the crossbar (x-bar) does the signal selection, and its output is also 14-bit. The filter and window operate at 16-bit, and the FFT of this signal outputs 31-bit, which is then scaled to 24-bit. The visibilities have 48-bit double the bit size. The Frame builder stage compresses the bit range but also maintains a high dynamic range; the 48-bit fixed point is converted into a 32-bit floating point number; this is done just before the value is ready to be stored in a flash. The flash interface operates with 16-bit words, so each floating point number is sent to the flash in two 16-bit words.

4. NCLE Data Handling and Operations

The NCLE data can be broadly classified as science (SC) data and House-Keeping (HK) (telemetry) data. The NCLE science data outputs are three auto-correlated and six cross-correlated data (Three real and three imaginary parts) per frequency bin, per integration time. The HK data provides the health status of the NCLE system. The HK data are received via two communication channels: one is the Controller Area Network (CAN) bus, and the second is through Low-Voltage Differential Signal (LVDS) bus. The cadence of the HK data from both methods is different; one provides real-time data while the other is batch-processed. The CAN housekeeping (CAN-HK) data gives us a real-time health check; the cadence of CAN-HK is every 2 s; in total, 14 HK blocks are defined, and depending on the operating mode, NCLE cycles through these blocks. The LVDS is the main interface to transmit large data output from NCLE to the platform. The LVDS handles four data types: batch-processed housekeeping, deployment, file, and direct experiment science data. LVDS housekeeping (LVDS-HK) data packets are generated by NCLE internally every 10 s. NCLE sends, every 60 s, packaged housekeeping data (6 packets) over LVDS to the satellite platform. The LVDS-HK data contains detailed information about the state of NCLE. Table 6 summarizes the cadence and volumes of each data from NCLE.

The DRS data is formatted into frames as part of the data download process to ground; this formatting gives us the NCLE data frame. The DRS data is defined as a block that is 16,384-byte (16 kB) in size. The bottom block (dark gray) in Figure 37 shows the DRS data block. Each 16 kB page starts with a 32-byte header that contains meta

information such as the page number, experiment number, and timestamps. The first DRS data block starts with an experiment header, which is 128 bytes in length. This header contains the experiment and system configuration details, such as X-bar mode, Filter, Window, FFT, FFT scaling, and other sub-system configurations from LNA, AIS, and calibrator configuration during the experiments. Each experiment data ends with 4 CRC bytes. The standard DRS data block is defined as 16 kB; if the experiment data size is smaller than 16 kB, filler data ('FF') is added to match the standard 16 kB size.

Table 6
NCLE Data Output Cadence and Data Volumes

NCLE data	Cadence	Data Volume	Interface
Real-Time HK	2 s	4 Bytes	CAN
Detailed HK	60 s	12 kBytes	LVDS
SC data	1.25 and ≤ 10 Mbps	-	LVDS

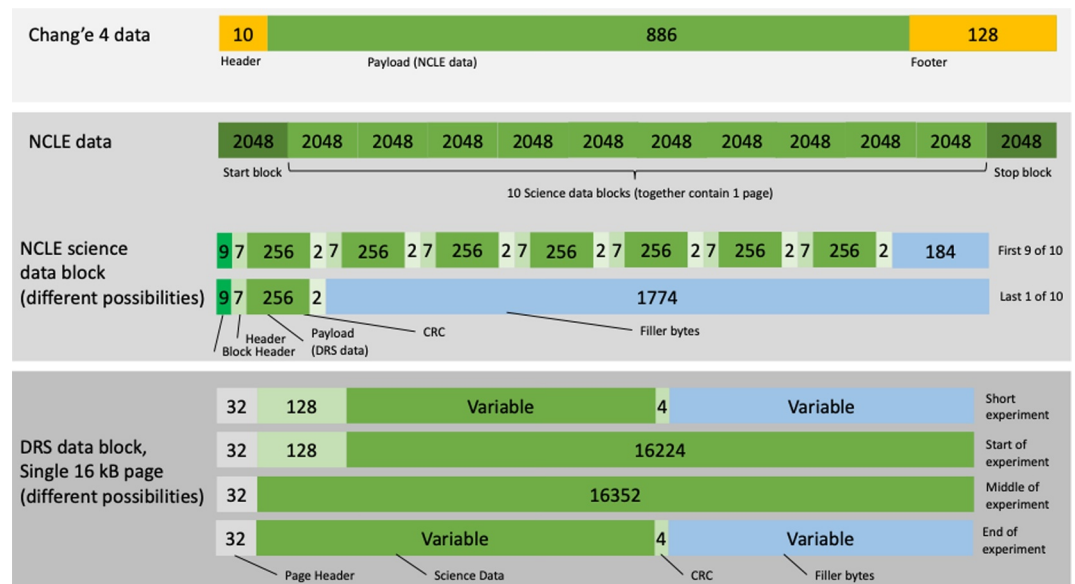


Figure 37. Schematic overview of data formatting to frames for download. The data framing order is from bottom to top: the bottom is the DRS 16 kB data, the middle is the 2048-byte block, and the top is the CE4 frame format (all numbers in the depictions of data blocks are expressed in bytes.).

A standard download data frame contains an arbitration field, control field, data field, CRC field, and acknowledgment field. The arbitration field contains header/identifier data and metadata. The metadata contains the experiment-related data such as time, page, and number. The data field contains the actual data. The frame ends with a CRC field. The LVDS protocol specification for the Chang'e 4 Data Transfer System (CE4-DTS) requires the data to be sent in frames of 2048-byte. The NCLE data has to be formatted to the frame size of 2048-byte; each 16 kB DRS data is formatted to fit the frame size of 2048-byte. This frame of 2048-byte is defined as

Table 7
An Example of a Preset Mode and Its Respective NCLE Settings

DRS ID	Description	mode		xbar		filter		window	nFFT	FFT scaling	int. Period		no. of Ints		
		Value	Desc.	Value	Desc.	Value	Value	Desc.	Value	Value	Desc.	Value	Value	num. Pages	num. Blocks
0	standard 60 MHz BW 1-s recording mode, 3s total, X&Y calibration	0	X,Y,Cal	0x07	pass-through	0x00	1	16k	0x0E	10	1 s	7000	3	54	1
1	standard 60 MHz BW 1-s recording mode, 600 s total	0	X,Y,Z	0x24	pass-through	0x00	1	16k	0x0E	10	1 s	7000	600	10,800	6
2	hi-res 60 MHz BW 0.1-s recording mode, 60 s total	0	X,Y,Z	0x24	pass-through	0x00	1	16k	0x0E	10	0.1 s	700	600	10,800	6
3	slow 60 MHz BW 10-s recording mode, 7200 s total	0	X,Y,Z	0x24	pass-through	0x00	1	16k	0x0E	10	10 s	70,000	720	12,960	7

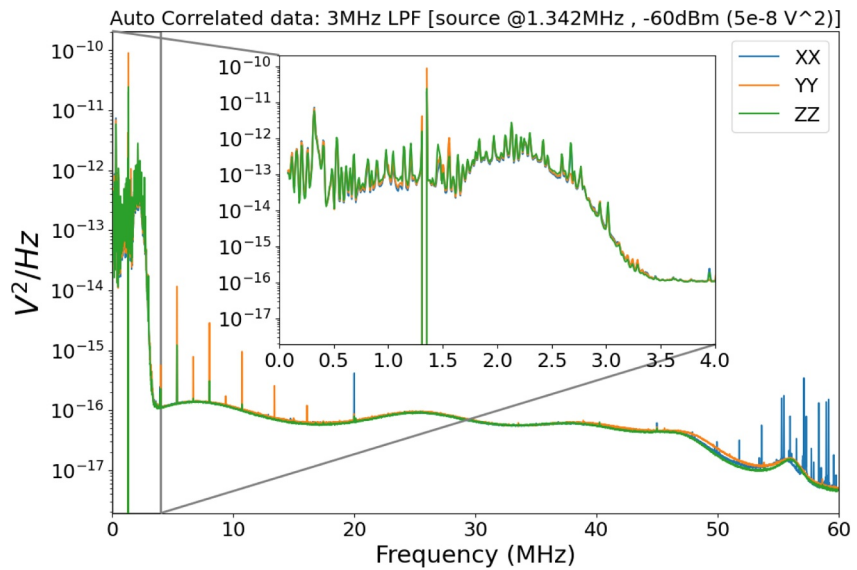


Figure 40. AC spectra with LNA connected to an external signal generator source, and LNA has 3 MHz LPF active (NCLE operating Band-1), the external source power is set at -60 dBm and frequency at 1.342 MHz. The AIS is in 1st Nyquist sampling zone.

For specific science cases, the NCLE subsystem must be configured with specific system settings (analog filter settings, attenuation settings, DRS input selection, FFT length, and number of integrations.). The specific science case settings are pre-loaded onto NCLE before launch and are efficiently executed by issuing the corresponding preset experiment commands. Table 7 shows an example of a science preset mode and the NCLE system configurations in that preset. The preset example 0, is the standard calibration experiment; when this preset is requested, the NCLE is configured, where X-bar is XYCAL, and Filter is set to 0–60 MHz (pass-through), Window is inactive with Blackman-Harris co-efficient being 1, FFT is with 16,384 points (16k- FFT), and FFT-scaling is set to 10, the integration time is 1 s. The experiment has three integration numbers, and each integration

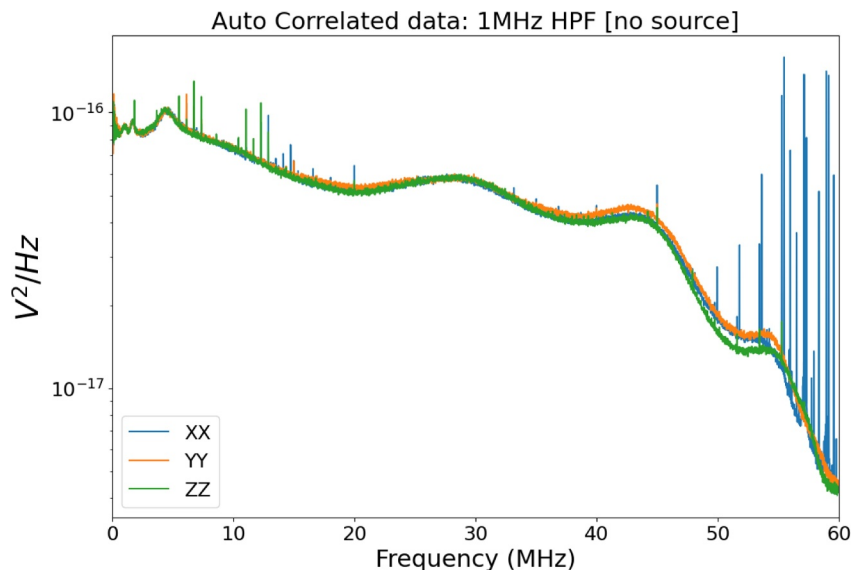


Figure 41. AC spectra with LNA terminated by 50 Ω load (no antenna case), and LNA has 1 MHz HPF active (NCLE operating Band-2).

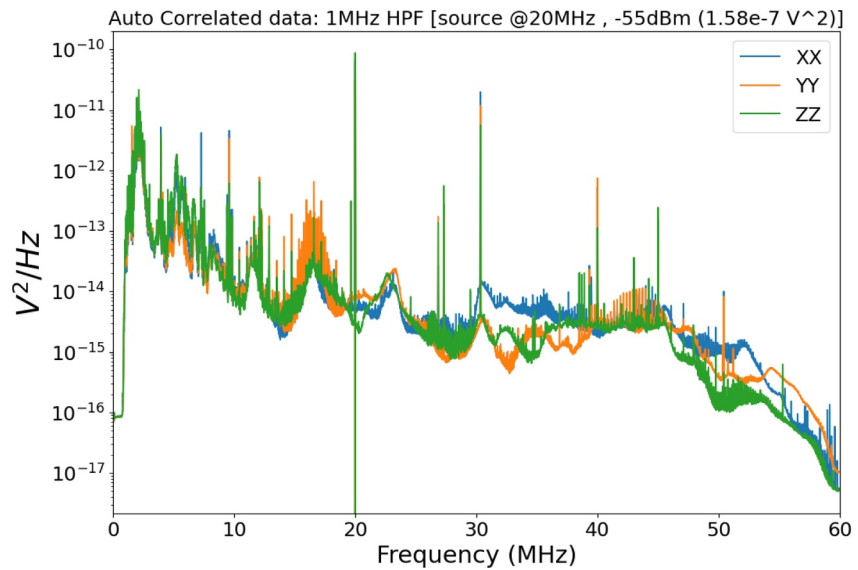


Figure 42. AC spectra with LNA connected to an external signal generator source, and LNA has 1 MHz HPF active (NCLE operating Band-2); the external source power is set at -55 dBm and frequency at 20.0 MHz. The AIS is in 1st Nyquist sampling zone.

is framed into a 18 DRS page; for the calibration experiment, the total data is framed in 54 DRS pages. The NCLE configuration is not just limited to pre-loaded presets; it can be custom-configured.

5. NCLE Integrated Spectra

This section presents the spectra measured on the ground after integrating NCLE subsystems. A sub-selection of the NCLE spectra from this integration test is presented here. Figure 38 shows the integration test setup, which is performed with the complete signal chain (analog and digital chain). For this test, an external source with very low output power (<-55 dBm) is used, and the frequency selection is made manually. The frequency value is chosen

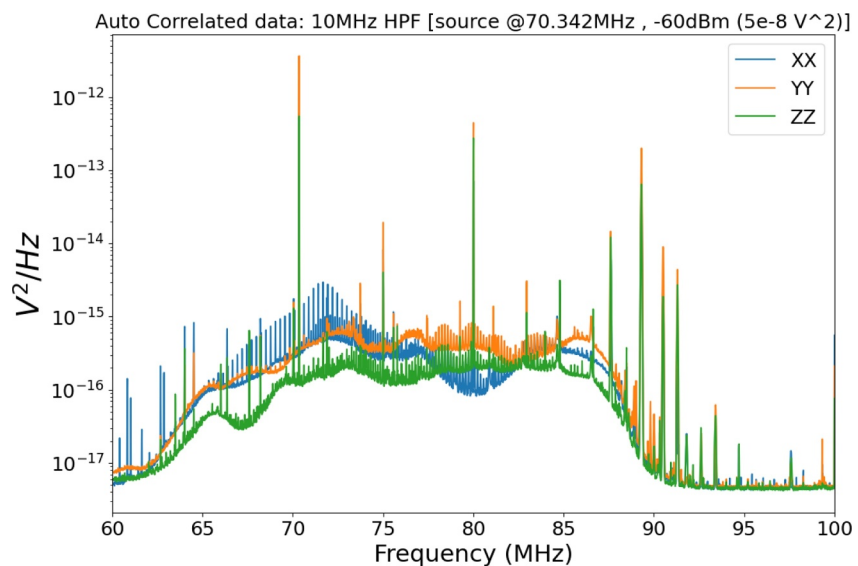


Figure 43. AC spectra with LNA connected to an external signal generator source, LNA has 10 MHz HPF active (Band-4), and the external source power is set at -60 dBm and frequency at 70.342 MHz. The AIS is in 2nd Nyquist sampling zone. The fine peaks observed at the noise floor are due to the EM emissions from the electrical components within the test environment; the spectra shown are not calibrated.

randomly and within the NCLE active operating frequency range for the selected NCLE mode. The DRS then digitizes the data as described in Section 3.4 to produce auto and cross-correlated outputs. Two tests are conducted per experiment: the first test is with the LNA terminated with a 50 Ω load (no antenna connected), and the second test is with a source connected to the LNA and an external source active. Figure 39 shows the AC spectra with LNA terminated by 50 Ω load (no antenna case) for Band-1 (see Table 3). Figure 40 shows the AC spectra with the antennas connected to the LNA, the AIS is in 1st Nyquist sampling zone, and LNA has 3 MHz LPF active (Band-1). The external source power is set at -60 dBm and frequency at 1.342 MHz. By comparing Figures 39 and 40, it is evident that NCLE system has captured this external source at 1.342 MHz. The external source is above the noise floor by >30 dBm. Figure 41 shows the AC spectra with LNA terminated by 50 Ω load (no antenna case) for Band-2. Figure 42 shows the AC spectra with the antennas connected to the LNA, the AIS is in 1st Nyquist sampling zone, and LNA has 1 MHz HPF active (Band-2). Here, the external source power is at -55 dBm and frequency at 20.0 MHz. By comparing Figures 41 and 42, it is evident that NCLE system has captured this external source at 20 MHz. The external source is above the noise floor by >30 dBm. Figure 43 shows the AC spectra with antennas connected, the AIS is in 2nd Nyquist sampling zone, and LNA has 10 MHz HPF active (Band-4), the external source power is set at -60 dBm and frequency at 70.342 MHz.

5.1. RFI Mitigation Measures

The primary RFI mitigation measure in the analog design was to make it as linear as possible. The Chang'e 4 satellite specifies it meets MIL-STD-461E. EMC measurements on a spacecraft engineering model with antenna monopole mock-ups mounted to the satellite showed relatively high levels, especially below 1 MHz. To address this, the input band was split into five bands, making it easier to design highly linear channels. The EMC measurements also showed a few DC-DC converter combs originating from power sources external to the spacecraft. This is also observed with the spectra from integration Figure 41. Anticipating DC-DC combs from the solar panels (not mounted for the tests), the receiver included high spectral resolution modes in order to be able to operate between the comb spikes. The NCLE subsystems are mounted in closed, filtered (power), metal boxes, and (ground) loops are avoided as much as possible. The LNA box is a Faraday cage; the RF coax is within a harness that is clamped on all sides without contacting the coax cables. The LNA board itself contains a bleeding resistor and ESD diode protection. An 80 kHz high-pass filter is placed in series. DC powers are filtered in common-mode and differential mode. Radiated and conducted emission tests were performed with NCLE FM model according to MIL standard 461G, test CE102 during integration (see Figure 12 from Hernandez et al. (2019)), which showed few DC-DC converter combs at higher frequencies; however, the noisiest still was the band below 1 MHz.

6. Conclusion

NCLE is a low-frequency instrument designed, developed, tested, and integrated within a quite short development time of 2 years. This paper discusses in depth the complete NCLE signal chain, the digital receiver system, and performances, adding more details to what has been presented in the previous papers about ground integration test results (Hernandez et al., 2019), EMI mitigation (Prinsloo et al., 2018) and antenna design (Arts et al., 2019). The achieved instrument performances, measured through ground tests, are at par with the initial requirements. The typical spectral noise level at the output of NCLE is -130 dBm/Hz for frequencies close to 15 MHz. This translates to a system equivalent flux density (SEFD) of $2 \cdot 10^{-22} \text{Wm}^{-2} \text{Hz}^{-1}$ (with 5 m antenna) (see Appendix B), which also matches the theoretical sensitivity (Figure 7). The expected fluctuation in power spectral density across a significant part of the Galactic spectrum (relatively close to the peak of Galactic emission at 3 or 4 MHz) is detectable by NCLE. Measuring the Jupiter Decametric emission is also possible with NCLE. Assuming NCLE configuration with an integration time of 0.1 s (per spectra), a total observation time of 300 s, a 9x decimation setting, and selecting the subband from 26.66 to 33.33 MHz provides an SNR of 11 dB. The same configuration with an integration time of 10 s and a total observation time of 30,000 s provides an SNR of 16 dB.

One of the primary purposes of NCLE is to demonstrate the possibilities of science at low frequency in the near Moon environment and formulate new technical requirements for future radio instruments. A future paper will present the results of commissioning activities performed on flight and details of instrument calibration.

NCLE is a fully configurable instrument. Pre-loaded configurations have been designed to support the science observation plan. Work is underway to implement and perform a software update that will extend the number of these configurations.

Appendix A: Cross-Correlated Data

Figure A1 shows the CC spectra with LNA terminated by $50\ \Omega$ load (no antenna case) for Band-1 (see Table 3). Figure A2 shows the CC spectra with the antennas connected to the LNA, the AIS is in 1st Nyquist sampling zone, and LNA has 3 MHz LPF active (Band-1). The external source power is set at $-60\ \text{dBm}$ and frequency at 1.342 MHz. Figure A3 shows the CC spectra with LNA terminated by $50\ \Omega$ load (no antenna case) for Band-2. Figure A4 shows the CC spectra with the antennas connected to the LNA, the AIS is in 1st Nyquist sampling zone, and LNA has 1 MHz HPF active (Band-2). Here, the external source power is at $-55\ \text{dBm}$ and frequency at 20.0 MHz. Figure A5 shows the AC spectra with antennas connected, the AIS is in 2nd Nyquist sampling zone, and LNA has 10 MHz HPF active (Band-4), the external source power is set at $-60\ \text{dBm}$ and frequency at 70.342 MHz.

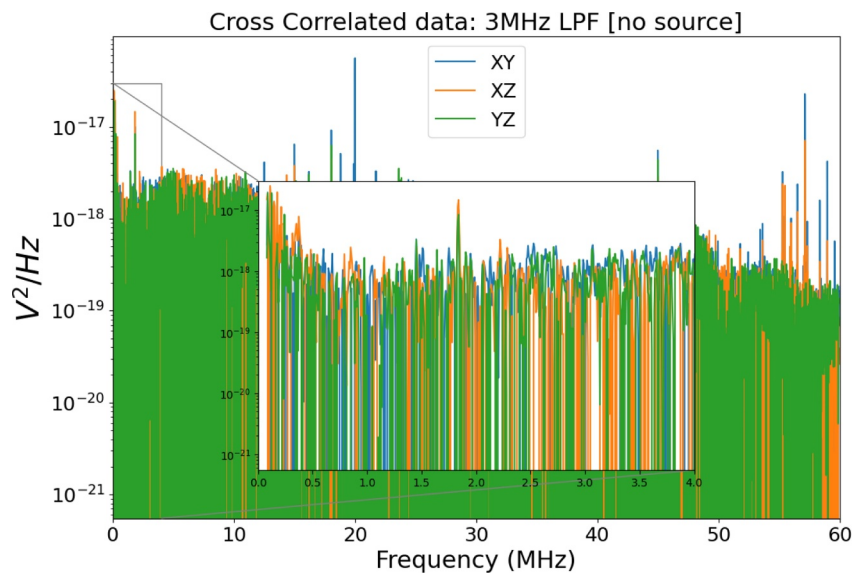


Figure A1. Cross-correlated (CC) spectra are measured on the ground after integrating the NCLE subsystems. AC spectra with LNA terminated by $50\ \Omega$ load (no antenna case). The fine peaks observed at the noise floor are due to the EM emissions from the electrical components within the test environment; the spectra shown are not calibrated.

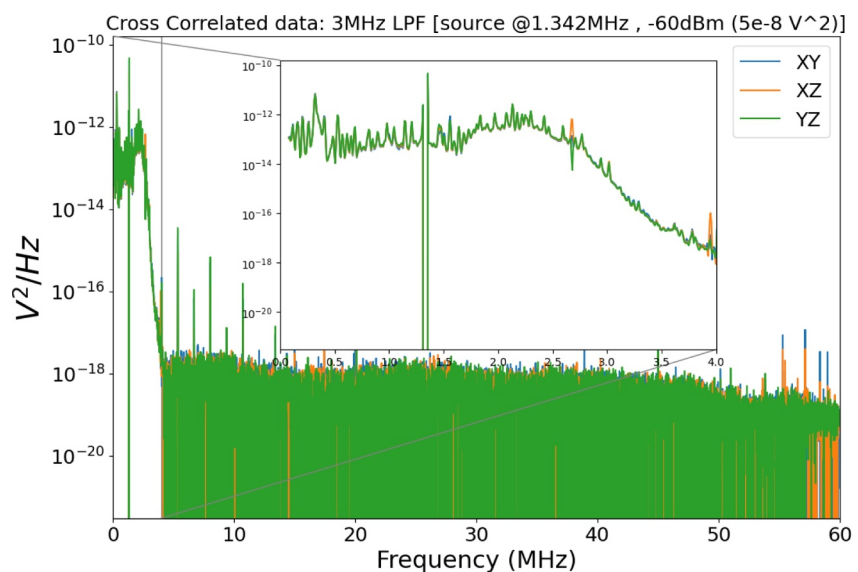


Figure A2. CC spectra with LNA connected to an external signal generator source, and LNA has 3 MHz LPF active (NCLE operating Band-1), the external source power is set at $-60\ \text{dBm}$ and frequency at 1.342 MHz. The AIS is in 1st Nyquist sampling zone.

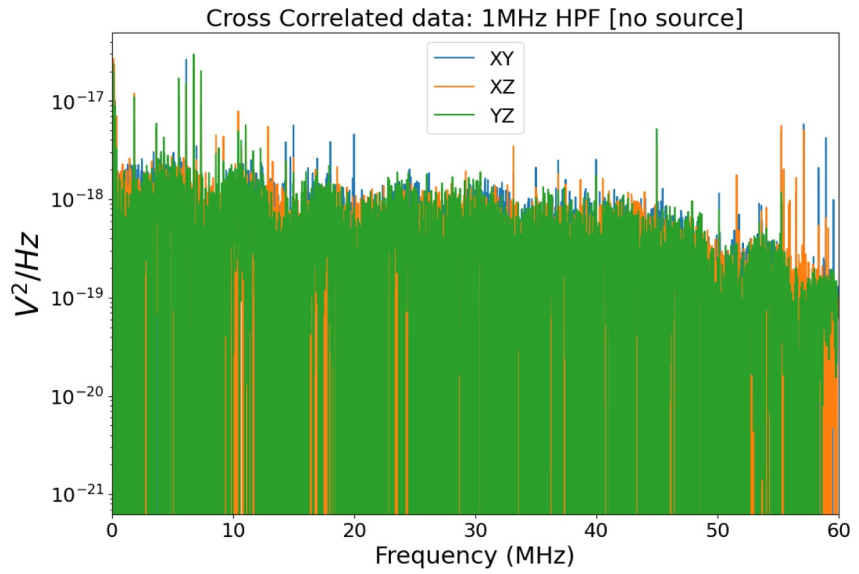


Figure A3. CC spectra with LNA terminated by 50 Ω load (no antenna case), and LNA has 1 MHz HPF active (NCLE operating Band-2).

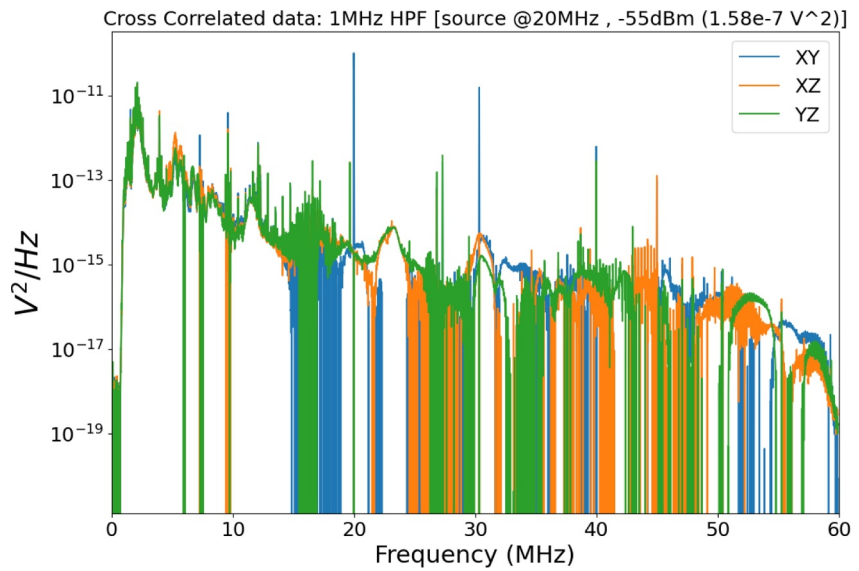


Figure A4. CC spectra with LNA connected to an external signal generator source, and LNA has 1 MHz HPF active (NCLE operating Band-2); the external source power is set at -55 dBm and frequency at 20.0 MHz. The AIS is in 1st Nyquist sampling zone.

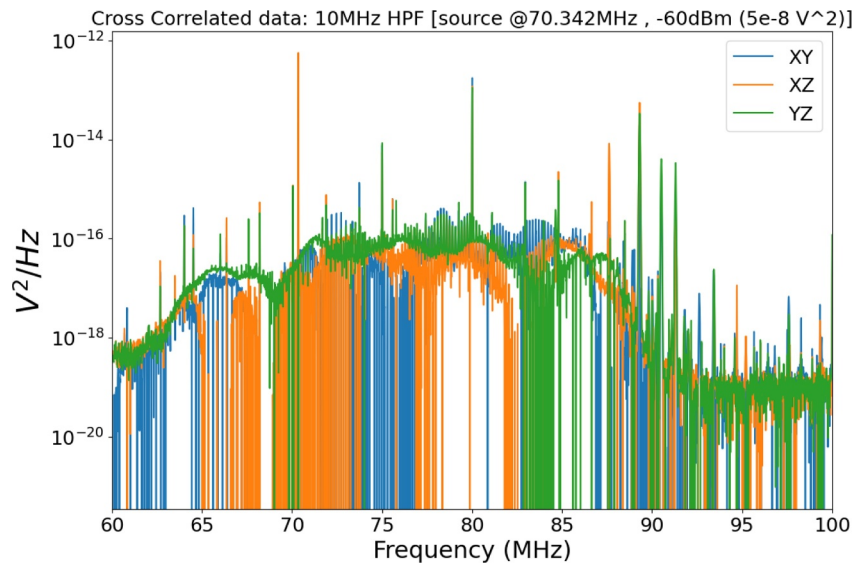


Figure A5. CC spectra with LNA connected to an external signal generator source, LNA has 10 MHz HPF active (Band-4), and the external source power is set at -60 dBm and frequency at 70.342 MHz. The AIS is in 2nd Nyquist sampling zone. The fine peaks observed at the noise floor are due to the EM emissions from the electrical components within the test environment; the spectra shown are not calibrated.

Appendix B: SEFD Calculations

The section presents the expected signal strength from the Galactic background measured by NCLE (R. Manning & Dulk, 2001) concluded that the Galactic center is brighter than the rest of the sky at frequencies above 4.7 MHz but not below. In order to distinguish the Galactic center, only frequencies above 4.7 MHz are considered in this calculation. At 15 MHz, an average brightness temperature of 10^5 K is expected and modulated at $\approx 13\%$.

The sky map at 45 MHz from (A. E. Guzman et al., 2011) shows brightness temperatures ranging from 4000/5000 K (outside of the Galactic plane) to 8000/10000 K in the Galactic plane and up to 54000 K toward the Galactic center. We use this map for elementary modeling of the expected signal (and its modulation) received by NCLE. Applying the temperature spectral index also stated in that paper (beta, which is approximately 2.2), we can extrapolate the brightness temperature down from 45 to 15 MHz and find that it should be a factor $\exp(2.2 \cdot \log(3)) = 11.2$ higher, making it a little over $6 \cdot 10^5$ K. This approach is considered valid as the peak of the Galactic background spectrum lies close to 3 or 4 MHz, with a clean power-law describing the spectral slope at higher frequencies. We therefore assume that the spectral index quoted in the paper above extends down to 15 MHz. This will be utilized as a verification tool in the subsequent calculations.

We model the entire sky as a distribution of discrete sources, each of which has an appropriate angular size (collectively, they cover the entire sky). The antenna response can be modeled as a simple dipole (donut) pattern, appropriately scaled by the expected sensitivity at the relevant frequency. An observing frequency of 15 MHz is chosen as this is close to the resonance frequency of the fully deployed NCLE antenna. From the brightness temperatures, the contribution of each sky 'pixel' is converted to Jansky, and the corresponding power picked up by the NCLE antenna is calculated. This is integrated over the entire sky to get the received spectral power. Then, the effect of the NCLE signal chain is added to get the measured power spectral density. The resulting spectra power density gives the expected noise levels that NCLE can measure.

The power spectral density can be obtained from the brightness temperature using the Rayleigh-Jeans law $T = \frac{\lambda^2}{2k\Omega} S$, where T is the brightness temperature, λ the wavelength, k the Boltzmann constant, Ω the beam solid angle and the S the flux density all in *mks* units. For example, a source with a 0.01 steradian solid angle, an observing frequency of 45 MHz, and a source brightness temperature of 600000 K gives a flux density S of $3.73 \cdot 10^{-21}$ W/m²/Hz which translates to 373000 Jy.

Table B1
Expected Power Spectral Density Variations and Voltage Variations for the Three Modulation Scenarios

Modulation	Maximum	Intermediate	Low
Spectral flux density modulation over 1 month [W/m ² /Hz]	$1.80 \cdot 10^{-21}$	$1.56 \cdot 10^{-21}$	$9.00 \cdot 10^{-22}$
Power spectral density modulation over 1 month ($A_{e,ff} = 100 \text{ m}^2$) [W/Hz]	$1.80 \cdot 10^{-19}$	$1.56 \cdot 10^{-19}$	$9 \cdot 10^{-20}$
ADC power spectral density modulation over 1 month (system gain = 17 dB) [mW/Hz]	$9.0 \cdot 10^{-15}$	$7.8 \cdot 10^{-15}$	$4.5 \cdot 10^{-15}$
Relative to NCLE noise floor of -130 dBm [dB]	19.5	18.9	16.5

The spectral power received by an antenna from all sources across the sky is of prime interest. As sources are from all directions, the antenna's effective area is required to calculate the power contribution received from each source. A naive calculation would be to assume a simple dipole sensitivity pattern, meaning that the effective area scales as $\cos^2(\theta)$, with its maximum inplane at $\theta = \Pi/2$ and then dropping to zero for $\theta = 0$ and $\theta = \Pi$. This \cos^2 pattern needs to be scaled by the effective aperture of the antenna at the relevant wavelength (for NCLE antenna, this is at its resonance frequency of 15 MHz, and its effective area is $\approx \lambda^2/4 = 100 \text{ m}^2$). The result of this calculation gives us the required total spectral power received per unit of bandwidth (in W/Hz) from the whole sky, corresponding to a particular antenna orientation. For just the single source, when it is located centrally in the main lobe of our antenna, a spectral power received of $[3.73 \cdot 10^{-21} \text{ (W/m}^2\text{/Hz)} \times 100 \text{ (m}^2\text{)}] = 3.73 \cdot 10^{-19} \text{ W/Hz}$. Expressed in dBm/Hz ($10 \log_{10}(\text{mW/Hz})$), this is -154 dBm/Hz . Considering the gain of the NCLE analog signal chain (17 dB in the default configuration), the noise level associated with this example source at the ADC inputs is -137 dBm/Hz .

For Galactic emission modulation when this simple approach is applied, according to R. Manning and Dulk, (2001); with an average brightness temperature of 10^5 K at 15 MHz, which is modulated at 13% when scanning with a dipole antenna oriented and rotating in the Ecliptic plane. The power density can be modeled as some excess brightness from the Galactic center at 13% of the average value, or 13000 K (we ignore the unlikely possibility that part of the brightness excess comes from the Galactic anticenter). As this result came from a dipole antenna of $2 \times 7.5 \text{ m}$ lying in the plane of the Ecliptic (with the Galactic center lying close to this plane as well), an assumption can be made that the angular resolution of this antenna is close to about 1.5 radians. Redeeming that the apparent size associated with the excess brightness is about 2 steradians allows us to estimate the flux density excess coming from the Galactic center, providing an estimate of the maximum modulation expected. This figure is $1.8 \cdot 10^{-21} \text{ W/m}^2\text{/Hz}$ or $1.8\text{e}5 \text{ Jy}$.

With the assumption of NCLE antenna effective aperture to be 100 m^2 ($\lambda^2/4$, at 15 MHz resonance), the expected modulation as measured by NCLE can be calculated. The antenna's orientation needs to be precisely known with respect to the celestial sphere. The orientation is not known in this case. For this purpose, three cases are considered: maximum modulation, if the antenna axis passes through the direction of the Galactic center in the sky at some point during the month; intermediate modulation (when the smallest angle between the antenna axis and the Galactic center direction is 30°) and low modulation (when the minimum angle is 60°). In all three cases, the difference in the received power spectral density between maximum exposure (Galactic center entirely in the main antenna beam, broadside) and minimum exposure (Galactic center closest to antenna null direction) are considered.

The nominal amplification by the analog signal chain in the default NCLE wide-band recording mode is 17 dB (with LNA and AIS attenuators set to 0 dB), meaning that the power scales by a factor of $10^{17/10} = 50$ as it is passed from antenna terminal to ADC terminal.

Table B1 presents the spectral flux density and power density modulation expected in each of the three cases. If the typical noise level measured by NCLE from space measurements is -130 dBm/Hz at frequencies close to 15 MHz, this corresponds to a power spectral density of $10^{-130/10} = 10^{-13} \text{ mW/Hz}$, or 10^{-16} W/Hz , at the ADC terminals. This is equivalent to a PSD of $2 \cdot 10^{-18} \text{ W/Hz}$ at the antenna terminal (assuming a gain of 17 dB for the analog signal chain). Assuming an effective antenna area of 100 m^2 and perfect efficiency, this is equivalent to a system equivalent flux density (SEFD) of $2 \cdot 10^{-22} \text{ W/m}^2\text{/Hz}$ or $2 \cdot 10^4 \text{ Jy}$. This number is significantly below the Galactic center excess of $1.8 \cdot 10^5 \text{ Jy}$. It also matches well with the SEFD at the 5 m antenna resonance calculated by ASTRON (see Figure 7). The last column of the table shows the relative strength of the Galactic background

modulation with respect to the NCLE noise floor. Even with a 10-fold reduction in sensitivity arising from reduced antenna length and a shift from antenna resonance, the Galactic background modulation should be easily detectable. From these results, the expected variation in power spectral density across a significant part of the spectrum (relatively close to the peak of Galactic emission at 3 or 4 MHz) should be detectable by NCLE.

List of Acronyms

ABP	Antenna Base Plate
ADC	Analog Digital Convertor
AIS	Analog Input Stage
AKR	Auroral Kilometric Radiation
BLDC	Brushless DC motor
BPF	Band Pass Filter
CAN	Controller Area Network
CD	Cosmic Dawn
CDHS	Command and Data Handling System
CE4-DTS	Chang'e 4 Data Transfer System
CFRP	Carbon Fibre Reinforced Plastic
CME	Coronal Mass Ejections
CMRR	Common-Mode Rejection Ratio
COTS	Commercial off-the-shelf
CRC	Code Redundancy Check
CSAC	Chip-Scale Atomic Clock,
DA	Dark Ages
DRS	Digital Receiver System
EBOX	Electronics BOX
EM	ElectroMagnetic field
EMC	Electromagnetic Compatibility
ENOB	Effective Number Of Bits EoR Epoch of Reionization
FFT	Fast Fourier Transform
FPGA	Field Programmable Gate Arrays
FWHM	Full-Width Half Maximum
GMRT	Giant Metrewave Radio Telescope
GSM	Global Sky Model
HK	House-Keeping
HPF	High Pass Filter
L2	Lagrange Point 2
LBA	Low Band Antenna
LCRT	Lunar Crater Radio Telescope

LFIS	Low Frequency Interferometer and Spectrometer
LNA	Low Noise Amplifier LOFAR Low-Frequency ARray
LPF	Low Pass Filter
LuSEE	Night Lunar Surface Electromagnetic Experiment-Night
LVDS	Low-Voltage Differential Signal
MSPS	Mega Samples per Second
MWA	Murchison Widefield Array
NCLE	Netherlands-China Low-Frequency Explorer
NF	Noise Figure
OCXO	Clock
OIP3H	higher output third-order intercept point harmonic
OIP3L	lower output third-order intercept point harmonic
OPAMP	Operational Amplifier
P1dB	Input-referred 1 dB compression point
PAPER	Precision Array to Probe the Epoch of Reionization
PCB	Printed Circuit Board
PFD	Power Flux Density
PSRR	Power Supply Rejection Ratio
PSU	Power Supply Unit
QTN	Quasi Thermo Noise
RAE	Radio Astronomy Explorers
RF	Radio Frequency
RFI	Radio Frequency Interference
RFS	Radio Frequency Spectrometer
RMS	Root Mean Square
ROLSSES	Radiowave Observations at the Lunar Surface of the photoElectron Sheath
RPW	Radio Plasma Wave
SKALA	Square-Kilometre Array
SMA	Sub-Miniature version A
SNR	Signal to Noise Ratio
SPP	Solar Probe Plus
TCU	Thermal Control unit
ULW	Ultra-Long-Wavelength
VLBI	Very Long Baseline Interferometry
VSWR	Voltage Standing Wave Ratio

Data Availability Statement

Data sets used for this research are available at Karapakula et al. (2024) repository, Zenodo via <https://doi.org/10.5281/zenodo.11403360> with open access.

Acknowledgments

NCLE team acknowledges the Netherlands Foundation for Scientific Research (NWO) for Grant 629.001.021. NCLE team acknowledges the support from the ESA/ESTEC PRODEX team for engineering support, review, and feedback during the development phase. NCLE team is grateful for the engineering support from the Netherlands Institute for Space Research (SRON) and Royal Netherlands Aerospace Centre (NLR). NCLE team greatly appreciates the embedded software support provided by Inspiro B.V. for the Digital Receiver. NCLE teams also acknowledge the SCS-Space company in South Africa for providing the demo hardware for the receiver prototyping. NCLE team thanks Hanna Rothkaehl from Centrum Badan Kosmicznych PAN (CBK) for providing us with the digital receiver of the RELEC mission to test the NCLE analog chain during development. NCLE team acknowledges the support from the Netherlands embassy in China for logistical and translation support. French co-authors acknowledge support from CNES (Centre National d'Etudes Spatiales), CNRS (Centre National de la Recherche Scientifique), and Observatoire de Paris-PSL.

References

- Alexander, J. K., Kaiser, M. L., Novaco, J. C., Grena, F. R., & Weber, R. R. (1975). Scientific instrumentation of the Radio-Astronomy-Explorer-2 satellite. *Astronomy & Astrophysics*, *40*(4), 365–371.
- Alvarez, H., Aparici, J., May, J., & Olmos, F. (1997). A 45-mhz continuum survey of the southern hemisphere. *Astronomy & Astrophysics, Supplement Series*, *124*(2), 315–328. <https://doi.org/10.1051/aas:1997196>
- Arts, M. J., Prinsloo, D. S., Ruiter, M., & Boonstra, A. J. (2019). Design of a reconfigurable array of monopoles for The Netherlands china low-frequency explorer. In *2019 13th eu-ropian conference on antennas and propagation (euacap)* (pp. 1–5).
- Backer, D. C., Parsons, A., Bradley, R., Parashare, C., Gugliucci, N., Mastrantonio, E., & Aguirre, J. (2007). Paper: The precision array to Probe the epoch of reionization. *American astronomical society meeting abstracts*, *211*, 133.02.
- Bale, S. D., Bassett, N., Burns, J. O., Dorigo Jones, J., Goetz, K., Hellum-Bye, C., & Suzuki, A. (2023). LuSEE 'night': The lunar surface electromagnetics experiment. *arXiv e-prints*. <https://doi.org/10.48550/arXiv.2301.10345>
- Benediktov, E., Getmantsev, G., Sazonov, Y., & Tarasov, A. (1965). Preliminary results of measurements of the intensity of distributed extra-terrestrial radio frequency emission at 725 and 1525 khz. *Kosmicheskie Issledovania*, *3*.
- Boonstra, A., Wise, M., van der Marel, J., Ruiter, M., Arts, M., Prinsloo, D., & Rothkaehl, H. (2017). The Netherlands - China low frequency explorer. In *32nd ursi gass* (pp. 19–26). Retrieved from [https://www.ursi.org/proceedings/procGA17/papers/Paper_J19-2\(1603\).pdf](https://www.ursi.org/proceedings/procGA17/papers/Paper_J19-2(1603).pdf)
- Boudjada, M. Y., Galopeau, P. H. M., Lecacheux, A., & Rucker, H. (2013). Search for an eventual control of Saturnian kilometric radiation by Titan satellite. In *Egu general assembly conference abstracts*. EGU2013-1713. Retrieved from <https://ui.adsabs.harvard.edu/abs/2013EGUGA..15.1713B>
- Bougeret, J. L., Goetz, K., Kaiser, M. L., Bale, S. D., Kellogg, P. J., Maksimovic, M., et al. (2008). S/WAVES: The radio and plasma wave investigation on the STEREO mission. *Space Science Reviews*, *136*(1), 487–528. <https://doi.org/10.1007/s11214-007-9298-8>
- Bougeret, J. L., Kaiser, M. L., Kellogg, P. J., Manning, R., Goetz, K., Monson, S. J., et al. (1995). Waves: The radio and plasma wave investigation on the wind spacecraft. *Space Science Reviews*, *71*(1), 231–263. <https://doi.org/10.1007/BF00751331>
- Burns, J. (2024). Radio astrophysics and cosmology from the moon. *American astronomical society meeting abstracts*, *56*, 200.01.
- Burns, J., Gopalswamy, N., Farrell, W. M., & Bradley, D. C. (2023). NASA's first radio telescope on the moon: Radio wave observations at the lunar surface of the photoElectron sheath (ROLSSES). *American astronomical society meeting abstracts*, *55*, 107.01.
- Carilli, C. L., & Rawlings, S. (2004). Motivation, key science projects, standards and assumptions. *New A. Rev.*, *48*(11–12), 979–984. <https://doi.org/10.1016/j.newar.2004.09.001>
- Caswell, J. L. (1976). A map of the northern sky at 10 MHz. *Monthly Notices of the Royal Astronomical Society*, *177*(3), 601–616. <https://doi.org/10.1093/mnras/177.3.601>
- Cecconi, B. (2014). Goniopolarimetry: Space-borne radio astronomy with imaging capabilities. *Comptes Rendus Physique*, *15*(5), 441–447. <https://doi.org/10.1016/j.crhy.2014.02.005>
- Cecconi, B., Bonnin, X., Hoang, S., Maksimovic, M., Bale, S. D., Bougeret, J. L., et al. (2008). STEREO/Waves goniopolarimetry. *Space Science Reviews*, *136*(1–4), 549–563. <https://doi.org/10.1007/s11214-007-9255-6>
- Cecconi, B., Bougeret, J.-L., Zarka, P., Thidé, B., Bergman, J., Falcke, H., & Gizani, N. (2012). Radio astronomy from the moon. *COSPAR Information Bulletin*, *282*.
- Cecconi, B., Lamy, L., Zarka, P., Prange, R., Kurth, W. S., & Louarn, P. (2009). Go-niopolarimetric study of the revolution 29 perikrone using the cassini radio and plasma wave science instrument high-frequency radio receiver. *Journal of Geophysical Research*, *114*(A3). <https://doi.org/10.1029/2008JA013830>
- Chen, L., Ping, J., Falcke, H., & Wolt, M. K., & NCLE Team. (2020). The Netherlands- China low frequency explorer (NCLE). *American astronomical society meeting abstracts #236*, *236*, 102.03. Retrieved from <https://ui.adsabs.harvard.edu/abs/2020AAS...23610203C/abstract>
- Condon, J., & Ransom, S. (2016). *Essential radio astronomy*. Princeton University Press.
- Cordes, J. M. (1990). Low frequency interstellar scattering and pulsar observations. In N. E. Kassim & K. W. Weiler (Eds.), *Low frequency astrophysics from space* (pp. 165–174). Springer Berlin Heidelberg.
- Cordes, J. M. (2000). Interstellar scattering: Radio sensing of deep space through the turbulent interstellar medium. *Geophysical Monograph Series*, *119*, 105–114. <https://doi.org/10.1029/GM119p0105>
- de Lera Acedo, E., Razavi-Ghods, N., Troop, N., Drought, N., & Faulkner, A. J. (2015). SKALA, a log-periodic array antenna for the SKA-low instrument: Design, simulations, tests and system considerations. *Experimental Astronomy*, *39*(3), 567–594. <https://doi.org/10.1007/s10686-015-9439-0>
- De Oliveira-Costa, A., Tegmark, M., Gaensler, B. M., Jonas, J., Landecker, T. L., & Reich, P. (2008). A model of diffuse Galactic radio emission from 10 MHz to 100 GHz. *Monthly Notices of the Royal Astronomical Society*, *388*(1), 247–260. <https://doi.org/10.1111/j.1365-2966.2008.13376.x>
- Desch, M. D., & Rucker, H. O. (1983). The relationship between saturn kilometric radiation and the solar wind. *Journal of Geophysical Research*, *88*(A11), 8999–9006. <https://doi.org/10.1029/JA088iA11p08999>
- Dulk, G. A., Erickson, W. C., Manning, R., & Bougeret, J.-L. (2001). Calibration of low-frequency radio telescopes using the galactic background radiation. *Astronomy & Astrophysics*, *365*(2), 294–300. <https://doi.org/10.1051/0004-6361:20000006>
- Falcke, H. D., van Haarlem, M. P., de Bruyn, A. G., Braun, R., Ro'tgering, H. J., Stappers, B., et al. (2006). A very brief description of lofar – The low frequency array. *Proceedings of the International Astronomical Union*, *2*(14), 386–387. <https://doi.org/10.1017/S174392130701112X>
- Goel, A., Pisanti, D., McGarey, P., Gupta, G., Arya, M., Chahat, N., & Bandyopadhyay, S. (2022). Ultra-long wavelength radio astronomy using the Lunar Crater Radio telescope (LCRT) on the farside of the moon. *American astronomical society meeting #240*, *54*, 312.06.
- Gurnett, D. A. (1974). The earth as a radio source: Terrestrial kilometric radiation. *Journal of Geophysical Research (1896-1977)*, *79*(28), 4227–4238. <https://doi.org/10.1029/JA079i028p04227>
- Guzma'n, A. E., May, J., Alvarez, H., & Maeda, K. (2011). All-sky galactic radiation at 45 mhz and spectral index between 45 and 408 mhz. *Astronomy & Astrophysics*, *525*, A138. <https://doi.org/10.1051/0004-6361/200913628>

- Hernandez, P., Bertels, E., Fernandez, M., Ruiter, M., Visser, K., & Wolt, M. K. (2019). Technology demonstration of using cubesat methodologies for power control and distribution in a radio-astronomy instrument within the chang'e 4 mission. In *2019 european space power conference (espc)* (pp. 1–8). <https://doi.org/10.1109/ESPC.2019.8932041>
- Intema, H. T., van der Tol, S., Cotton, W. D., Cohen, A. S., van Bommel, I. M., & Rottgering, H. J. A. (2009). Ionospheric calibration of low frequency radio interferometric observations using the peeling scheme - I. method description and first results. *Astronomy & Astrophysics*, *501*(3), 1185–1205. <https://doi.org/10.1051/0004-6361/200811094>
- Ja'come, H. R. P., Marques, M. S., Zarka, P., Echer, E., Lamy, L., & Louis, C. K. (2022). Search for Jovian decametric emission induced by Europa on the extensive Nancy Decameter Array catalog. *Astronomy & Astrophysics*, *665*, A67. <https://doi.org/10.1051/0004-6361/202244246>
- Jester, S., & Falcke, H. (2009). Science with a lunar low-frequency array: From the dark ages of the universe to nearby exoplanets. *New Astronomy Reviews*, *53*(1), 1–26. <https://doi.org/10.1016/j.newar.2009.02.001>
- Jia, Y., Zou, Y., Ping, J., Xue, C., Yan, J., & Ning, Y. (2018). The scientific objectives and payloads of chang'e-4 mission. *Planetary and Space Science*, *162*, 207–215. <https://doi.org/10.1016/j.pss.2018.02.011>
- Kaiser, M. L. (1987). The first radio astronomy from space: Rae. In K. W. Weiler (Ed.), *Radio astronomy from space* (pp. 227–238).
- Kaiser, M. L., Desch, M. D., Bougeret, J. L., Manning, R., & Meetre, C. A. (1996). WIND/WAVES observations of man-made radio transmissions. *Geophysical Research Letters*, *23*(10), 1287–1290. <https://doi.org/10.1029/95GL03665>
- Karapakula, S. K., Brinkerink, C., Vecchio, A., Poushaghghi, H., Bertels, E., Klein-Wolt, M., & Falcke, H. (2024). The Netherlands - China Low Frequency Explorer signal chain pre launch test-data. (version 1.0) [Dataset]. *Zenodo*. <https://doi.org/10.5281/zenodo.11403359>
- Kassim, N. E., & Weiler, K. W. (1990). Low frequency astrophysics from space: Proceedings of an international workshop held in crystal city, Virginia, USA, on 8 and 9 January 1990 (Vol. 362). <https://doi.org/10.1007/3-540-52891-1>
- Kelley, M. C. (2009). *The earth's ionosphere: Plasma physics and electrodynamics*. Academic press.
- Klein Wolt, M., Aminaei, A., Zarka, P., Schrader, J.-R., Boonstra, A.-J., & Falcke, H. (2012). Radio astronomy with the european lunar lander: Opening up the last un-explored frequency regime. *Planetary and Space Science*, *74*(1), 167–178. <https://doi.org/10.1016/j.pss.2012.09.004>
- Koopmans, L., Barkana, R., Bentum, M., Bernardi, G., Boonstra, A.-J., Bowman, J., & Zarka, P. (2019). Peering into the dark (ages) with low-frequency space interferometers. *arXiv e-prints*, *arXiv:1908.04296*. <https://doi.org/10.48550/arXiv.1908.04296>
- Koopmans, L. V. E., Barkana, R., Bentum, M., Bernardi, G., Boonstra, A.-J., Bowman, J., et al. (2021). Peering into the dark (ages) with low-frequency space interferometers. *Experimental Astronomy*, *51*(3), 1641–1676. <https://doi.org/10.1007/s10686-021-09743-7>
- Kurth, W. S., Gurnett, D. A., Clarke, J. T., Zarka, P., Desch, M. D., Kaiser, M. L., et al. (2005). An Earth-like correspondence between Saturn's auro-ral features and radio emission. *Nature*, *433*(7027), 722–725. <https://doi.org/10.1038/nature03334>
- Maeda, K., Alvarez, H., Aparici, J., May, J., & Reich, P. (1999). A 45-mhz continuum survey of the northern hemisphere. *Astronomy & Astrophysics, Supplement Series*, *140*(2), 145–154. <https://doi.org/10.1051/aas:1999413>
- Maksimovic, M., Bale, S. D., Chust, T., Khotyaintsev, Y., Krasnosel'skikh, V., Kretzschmar, M., et al. (2020). The solar orbiter radio and plasma waves (rpw) instrument. *Astronomy & Astrophysics*, *642*, A12. <https://doi.org/10.1051/0004-6361/201936214>
- Maksimovic, M., Soucek, J., Chust, T., Khotyaintsev, Y., Kretzschmar, M., Bonnín, X., et al. (2021). First observations and performance of the rpw instrument on board the solar orbiter mission. *Astronomy & Astrophysics*, *656*, A41. <https://doi.org/10.1051/0004-6361/202141271>
- Manning, R., & Dulk, G. A. (2001). The Galactic background radiation from 0.2 to 13.8 MHz. *Astronomy & Astrophysics*, *372*(2), 663–666. <https://doi.org/10.1051/0004-6361:20010516>
- Meyer-Vernet, N. (1979). On natural noises detected by antennas in plasmas. *Journal of Geophysical Research*, *84*(A9), 5373–5377. <https://doi.org/10.1029/JA084iA09p05373>
- Mimoun, D., Wiczcerek, M. A., Alkalai, L., Banerdt, W. B., Baratoux, D., Bougeret, J.-L., et al. (2012). Farside explorer: Unique science from a mission to the farside of the moon. *Experimental Astronomy*, *33*(2), 529–585. <https://doi.org/10.1007/s10686-011-9252-3>
- Morales, M. F. (2005). Design principles of the Mileura wide-field array low frequency demonstrator (MWA-LFD). In N. Kassim, M. Perez, W. Junor, & P. Henning (Eds.), *From clark lake to the long wavelength array: Bill erickson's radio science* (Vol. 345, p. 452).
- Morales, M. F., Bowman, J. D., Cappallo, R., Hewitt, J. N., & Lonsdale, C. J. (2006). Statistical EOR detection and the Mileura Widefield array. *New A. Rev.*, *50*(1–3), 173–178. <https://doi.org/10.1016/j.newar.2005.11.033>
- Novaco, J. C., & Brown, L. W. (1978). Nonthermal galactic emission below 10 mega-hertz. *Astrophysical Journal*, *221*, 114–123. <https://doi.org/10.1086/156009>
- Prinsloo, D., Ruiter, M., Arts, M., Marel, J. V. D., Boonstra, A., Kruihof, G., & Ping, J. (2018). Emi modelling of an 80 khz to 80 mhz wideband antenna and low-noise amplifier for radio astronomy in space. In *12th European conference on antennas and propagation (eucaap 2018)* (pp. 1–4). <https://doi.org/10.1049/cp.2018.0820>
- Pulupa, M., Bale, S. D., Bonnín, J. W., Bowen, T. A., Carruth, N., Goetz, K., et al. (2017). The solar probe plus radio frequency spectrometer: Measurement requirements, analog design, and digital signal processing. *Journal of Geophysical Research (Space Physics)*, *122*(3), 2836–2854. <https://doi.org/10.1002/2016JA023345>
- Rajan, R. T., Boonstra, A.-J., Bentum, M., Klein-Wolt, M., Belien, F., Arts, M., et al. (2016). Space-based aperture array for ultra-long wavelength radio astronomy. *Experimental Astronomy*, *41*(1), 271–306. <https://doi.org/10.1007/s10686-015-9486-6>
- Rishbeth, H., & Garriott, O. K. (1969). Introduction to ionospheric physics.
- Roger, R. S., Costain, C. H., Landecker, T. L., & Swerdlyk, C. M. (1999). The radio emission from the galaxy at 22 mhz. *Astronomy & Astrophysics, Supplement Series*, *137*(1), 7–19. <https://doi.org/10.1051/aas:1999239>
- Rottgering, H. J. A., Braun, R., Barthel, P. D., van Haarlem, M. P., Miley, G. K., Morganti, R., & de Vos, C. M. (2006). Lofar - Opening up a new window on the universe. *arXiv*. <https://doi.org/10.48550/ARXIV.ASTRO-PH/0610596>
- Schilizzi, R. T. (2004). The square kilometer array. In M. Oschmann Jacobus (Ed.), *Ground-based telescopes*, (Vol. 5489, pp. 62–71). <https://doi.org/10.1117/12.551206>
- Swarup, G., Kapahi, V. K., Velusamy, T., Ananthakrishnan, S., Balasubramanian, V., & Kulkarni, V. K. (1991). Twenty-five years of radio astronomy at TIFR/tata institute for fundamental research. *Current Science*, *60*, 79.
- Thompson, A. R., Moran, J. M., & Swenson, G. W. (2001). *Interferometry and synthesis in radio astronomy*. Wiley. <https://doi.org/10.1002/9783527617845>
- van Haarlem, M. P., Wise, M. W., Gunst, A. W., Heald, G., McKean, J. P., Hessels, J. W. T., et al. (2013). Lofar: The low-frequency array. *Astronomy & Astrophysics*, *556*, A2. <https://doi.org/10.1051/0004-6361/201220873>
- van Harten, L., Jordans, R., & Pourshaghghi, H. (2017). Necessity of fault tolerance techniques in xilinx kintex 7 fpga devices for space missions: A case study. In *2017 euromicro conference on digital system design (dsd)* (pp. 299–306). <https://doi.org/10.1109/DSD.2017.45>
- Vecchio, A., Maksimovic, M., Krupar, V., Bonnín, X., Zaslavsky, A., Astier, P. L., et al. (2021). Solar orbiter/rpw antenna calibration in the radio domain and its application to type iii burst observations. *Astronomy & Astrophysics*, *656*, A33. <https://doi.org/10.1051/0004-6361/202140988>

- Wang, Q., & Liu, J. (2016). A chang'e-4 mission concept and vision of future Chinese lunar exploration activities. *Acta Astronautica*, *127*, 678–683. <https://doi.org/10.1016/j.actastro.2016.06.024>
- Wilson, T. L., Rohlfis, K., & Hu'temeister, S. (2013). *Tools of radio astronomy*. Springer Berlin. <https://doi.org/10.1007/978-3-642-39950-3>
- Yan, J., Wu, J., Gurvits, L. I., Wu, L., Deng, L., Zhao, F., et al. (2023). Ultra-low-frequency radio astronomy observations from a Seleno-centric orbit. *Experimental Astronomy*, *56*(1), 333–353. <https://doi.org/10.1007/s10686-022-09887-0>
- Zarka, P. (2020). *The low-frequency radio telescope Nenufar session j01 new telescopes on the frontier*. URSI GASS Rome. Retrieved from <https://tinyurl.com/ycocd5ly>
- Zarka, P., Bougeret, J.-L., Briand, C., Cecconi, B., Falcke, H., Girard, J., et al. (2012). Planetary and exoplanetary low frequency radio observations from the moon. *Planetary and Space Science*, *74*(1), 156–166. <https://doi.org/10.1016/j.pss.2012.08.004>
- Zarka, P., & Cecconi, B. (2022). Solar system low frequency radio spectra (version 1.0). [Dataset]. *PADC/MASER*. <https://doi.org/10.25935/YAWF-AF18>
- Zarka, P., Cecconi, B., & Kurth, W. S. (2004). Jupiter's low-frequency radio spectrum from cassini/radio and plasma wave science (rpws) absolute flux density measurements. *Journal of Geophysical Research*, *109*(A9). <https://doi.org/10.1029/2003JA010260>
- Zarka, P., Farges, T., Ryabov, B. P., Abada-Simon, M., & Denis, L. (1996). A scenario for jovian s-bursts. *Geophysical Research Letters*, *23*(2), 125–128. <https://doi.org/10.1029/95GL03780>
- Zarka, P., Marques, M. S., Louis, C., Ryabov, V. B., Lamy, L., Echer, E., & Cecconi, B. (2018). Jupiter radio emission induced by Ganymede and consequences for the radio detection of exoplanets. *Astronomy & Astrophysics*, *618*, A84. <https://doi.org/10.1051/0004-6361/201833586>